



Grant agreement n°: 825103
Call identifier: H2020-ICT-2018-2020

Customized photonic devices for defectless laser-based manufacturing

CUSTODIAN

Deliverable D1.1

Handbook on metallurgical defects and their genesis

Work Package 1

Definition of thermal cycles to reduce defect formation in SLM/LBW

Document type : Report
Version : V1
Date of issue : 14/11/2019
Dissemination level : PUBLIC
Lead beneficiary : PoliMi

This project has received funding from the European Union's Horizon 2020 research and innovation programme under grant agreement n° 825103. CUSTODIAN project is an initiative of the Photonics Public Private Partnership.



The dissemination of results herein reflects only the author's view and the European Commission is not responsible for any use that may be made of the information it contains.

The information contained in this report is subject to change without notice and should not be construed as a commitment by any members of the CUSTODIAN Consortium. The information is provided without any warranty of any kind.

This document may not be copied, reproduced, or modified in whole or in part for any purpose without written permission from the CUSTODIAN Consortium. In addition to such written permission to copy, acknowledgement of the authors of the document and all applicable portions of the copyright notice must be clearly referenced.

© COPYRIGHT 2019 The CUSTODIAN Consortium.

All rights reserved.



Executive Summary

Abstract	<p>Deliverable D1.1 of the Custodian Project gathers information on the features and mechanisms of generation of metallurgical defects that could be found after Laser powder bed fusion and Laser beam welding. Data are mainly obtained from a literature survey on available open publications.</p> <p>The reference materials for the project activities are the CM247LC and IN713LC alloys for LPBF and the AISI 304L austenitic stainless steel for LBW.</p>
Keywords	Literature survey, Ni-based superalloys, austenitic stainless steels, LPBF, LBW



Revision history

Version	Author(s)	Changes	Date
V1	Maurizio Vedani	-	14/11/2019
V2	Jorge Arias / Daniel Gesto / Francesco Stortiero	Peer Review	25/11/2019
V3	Maurizio Vedani	Final version	29/11/2019



TABLE OF CONTENTS

1	INTRODUCTION.....	5
2	NI-BASED ALLOYS AND LASER POWDER BED FUSION	5
2.1	Materials description	5
2.2	Principles of Laser powder bed fusion	10
2.3	Literature survey on LPBF of Ni-based superalloys.....	13
3	AUSTENITIC STAINLESS STEELS AND LASER BEAM WELDING	35
3.1	Austenitic stainless steels and their weldability	35
3.2	Literature survey on LBW of austenitic stainless steels.....	40
4	CONCLUSIONS.....	47
5	REFERENCES.....	48

1 INTRODUCTION

Deliverable D1.1 of the Custodian Project is meant to collect information on the features and mechanisms of generation of metallurgical defects found in laser powder bed fusion (LPBF) and laser beam welding (LBW) in the investigated alloys. Data are mainly obtained from a literature survey on available open publications.

The report can be disseminated without restrictions, it is available for download from the CUSTODIAN project website: <https://shapeyourlaser.eu/>

The reference materials for the project activities are the CM247LC and IN713LC alloys for LPBF and the AISI 304L austenitic stainless steel for LBW. The current report is organized into two parts, the first chapter concerns with LPBF while the second chapter involves LBW. Each of the two chapters contains a first section on description of reference materials and a summary about the main features of the corresponding processes, followed by a review of the most common properties and defects associated to them.

2 NI-BASED ALLOYS AND LASER POWDER BED FUSION

2.1 Materials description

Nickel-based superalloys are the main material choice for high-temperature applications, particularly when resistance to creep and fatigue is needed and the risk of degradation due to oxidation and/or corrosion is severe [1].

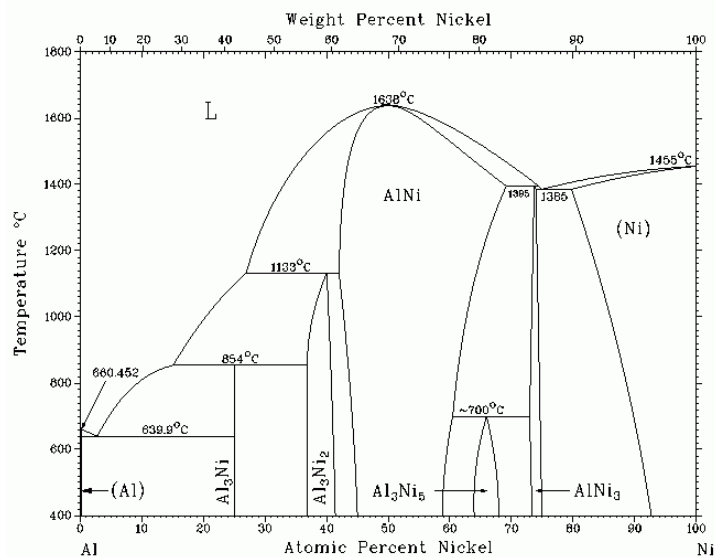
Some peculiar physical factors make Ni alloys particularly suitable for high temperature applications.

- The face-centered cubic (FCC) crystal structure shows no phase transformation up to melting point and their thermally activated processes controlling creep deformation are rather slow.
- There is a substantial solubility of alloying elements in the Ni matrix (γ -phase). Co, Fe, Cr, Ru, Mo, Re and W partition to it and tend to stabilize the γ -phase
- Ni is able to support the precipitation of the Ni_3Al γ' -phase, which exhibits the L12 crystal structure. Al, Ti, Nb and Ta have greater atomic radii and promote the formation of γ' (see figure 2.1).

- Grain boundary strengtheners such as C, B and Zr are used to confer the necessary time-dependent creep performance to polycrystalline superalloys. Cr, Mo, W, Nb, Ta and titanium are particularly strong carbide formers, Cr and Mo promote the formation of borides.

In Ni alloys, the FCC-type γ phase forms as a continuous matrix phase with significant concentrations of elements such as Co, Cr, Mo, Ru and Re in solid solution. The γ' phase, enriched in elements such as Al, Ti and Ta, usually precipitates as coherent particles within the γ -matrix (see figure 2.2). If Nb is present, the formation of ordered γ'' phase is predominant over the γ' phase.

Carbon, often present at concentrations up to 0.2 wt%, combines with reactive elements such as Ti, Ta and Hf to form MC carbides. During processing or service, these can decompose to other species such as $M_{23}C_6$ and M_6C , which prefer to reside on the γ -grain boundaries (GBs), and which are rich in Cr, Mo and W. B can combine with elements such as Cr or Mo to form borides, which reside on the γ -GBs as well.



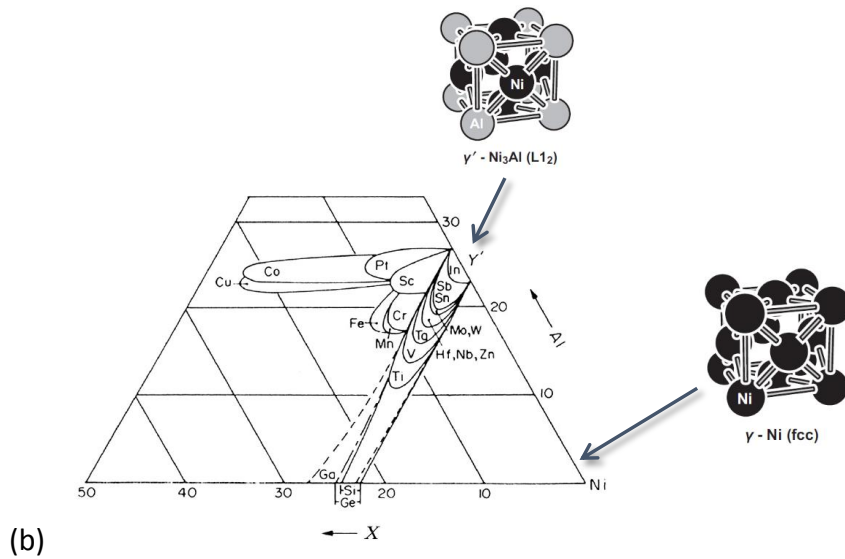


Figure 2.1: The binary Al-Ni phase diagram (a) and superimposed Al-Ni-X ternary diagrams showing modifications of the extent of the γ' phase field (b) [1]

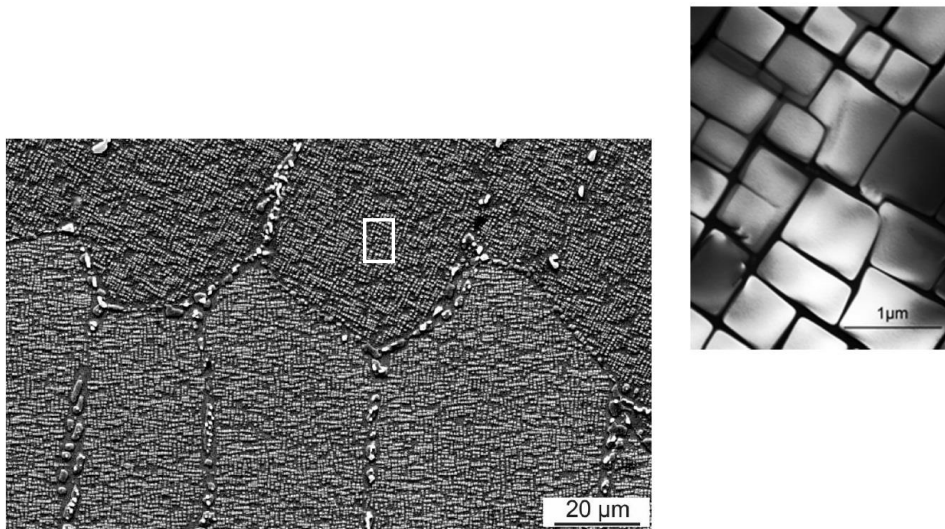


Figure 2.2. Microstructure of cast and heat treated Ni-based superalloy. The inset show the magnified aspect of the precipitated γ' phase [1]

The IN713LC and CM247LC alloys, are Ni-based casting materials featuring the composition reported in table 2.1. The expected room- and high-temperature tensile properties are listed in table 2.2. It is specified that the main strengthening mechanism is achieved by the precipitation of coherent precipitates of intermetallic phases Ni_3Al , or $\text{Ni}_3(\text{Al},\text{Ti})$ [4,5].

Table 2.1: Nominal chemical composition (wt.%) of the IN713LC and CM247LC alloys [4]

	C	Cr	Co	Mo	W	Ta	Nb	Al	Ti	Hf	Zr	B	Ni
IN713LC	0,05	12,0		4,5			2,0	5,9	0,6		0,1	0,01	bal.
CM247LC	0,07	8,0	9,3	0,5	9,5	3,2		5,6	0,7	1,4	0,010	0,015	bal.

Table 2.2: Expected mechanical properties of the IN713LC and CM247LC alloys [4]

	Temperature [°C]	UTS (MPa)	YS (MPa)	F.E. (%)	E (GPa)
IN713LC	RT	895	750	15	197
	538°C	895	760	11	172
CM247LC	RT	1242	1010	8,1	n.a.
	760°C	1200	1016	8,2	n.a.

From literature [11] it is known that for the 713LC alloy, γ' has the general formula $\text{Ni}_{2.95}\text{-Cr}_{0.95}\text{-Al}_{0.78}\text{-Ti}_{0.06}\text{-Nb}_{0.06}\text{-Mo}_{0.06}$. The γ' solvus is at 1205°C, while solidus and liquidus temperatures are at 1260°C and 1349°C, respectively. Finally, the chemical composition of MC carbides in Inconel-713LC is formulated as $(\text{Nb}_{0.4}\text{-Mo}_{0.25}\text{-Ti}_{0.18}\text{-Cr}_{0.16})\text{C}$.

Based on the given compositions, it is possible to predict the solidification and solid-phase transformation depicted in figures 2.3 and 2.4 for the IN713LC and CM247LC alloys, respectively. The data have been generated by the use of a thermodynamic simulation software (Thermo-Calc software AB) relying on the databases TCNi#8 version 8.2.

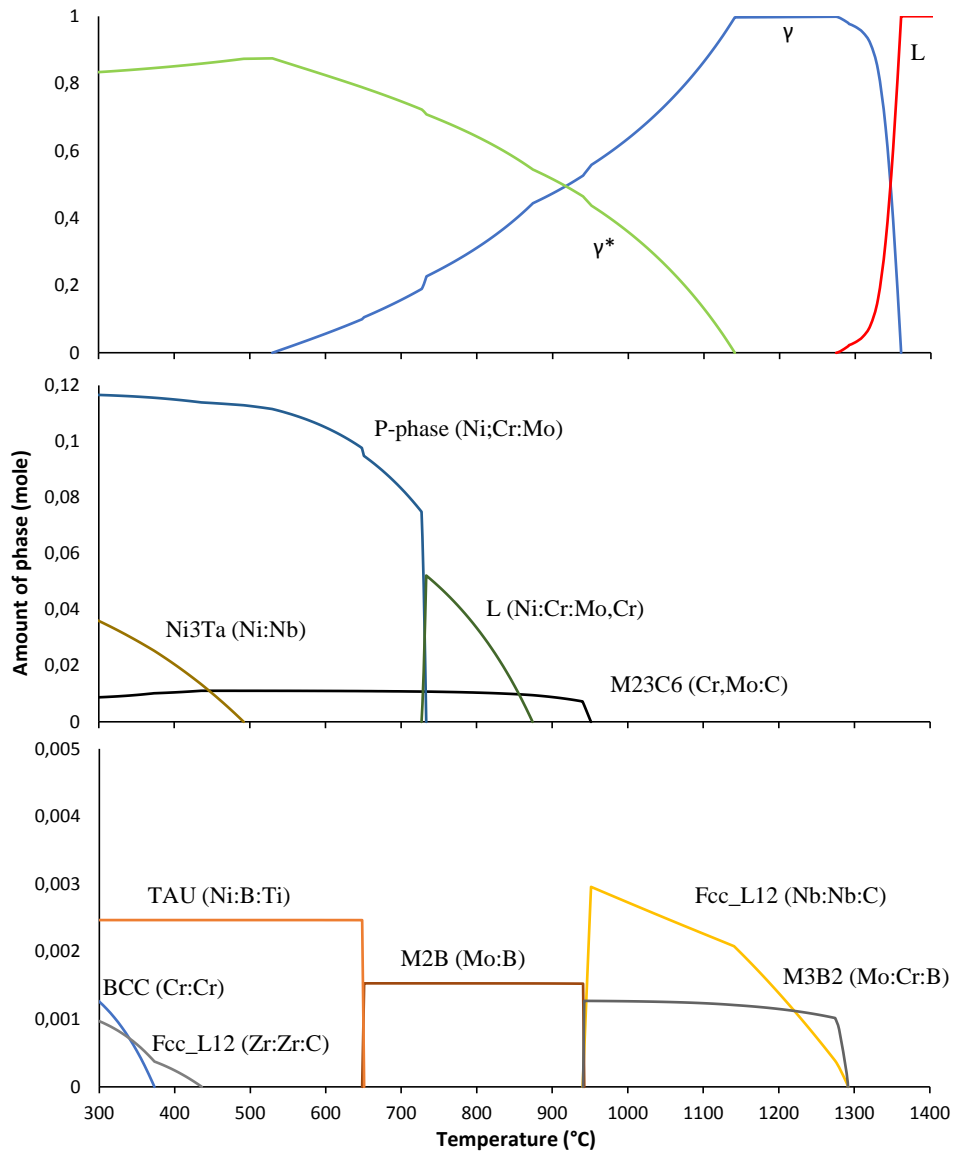


Figure 2.3: Calculated solidification curve and stability of phases vs. temperature for the IN713LC alloy

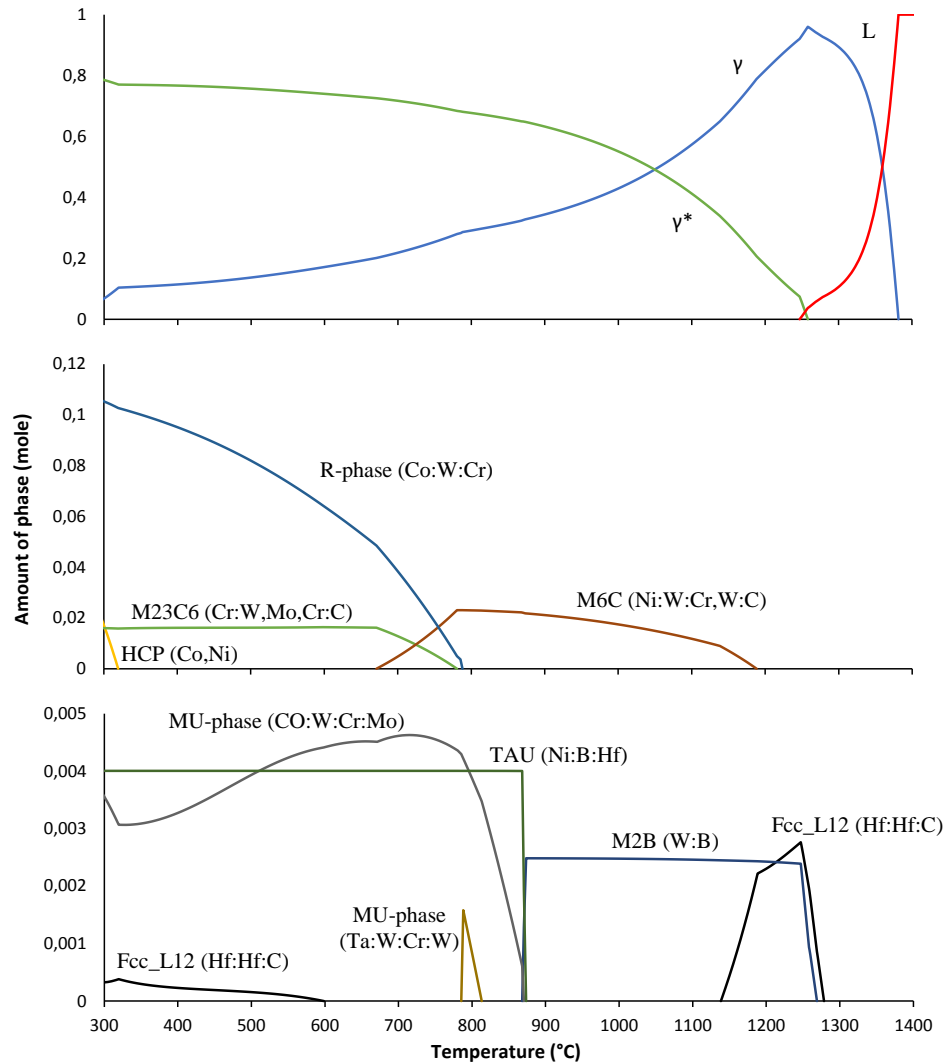


Figure 2.4: Calculated solidification curve and stability of phases vs. temperature for the CM247LC alloy

2.2 Principles of Laser powder bed fusion

Additive manufacturing (AM) processes build 3D parts by progressively adding thin layers of material driven by a digital model. In particular in the LPBF process a feedstock metal alloy in form of powder is consolidated into a dense metallic part by melting and solidification with the aid of a laser source in a layer by layer manner.

The process consists in drawing a CAD model, slicing it into planar layers and defining a scan path to generate the build-file. The part is then formed by spreading thin layers of powder and melting pass-by-pass and layers upon layer this powder under computer control, within

an inert chamber (see figure 2.6) [2]. Fusion occurs by the scanning motion of the laser heat source, resulting in melting and solidification of the overlapping tracks, according to a peculiar “multipass welding” approach, as confirmed by the resulting microstructure given in figure 2.7.

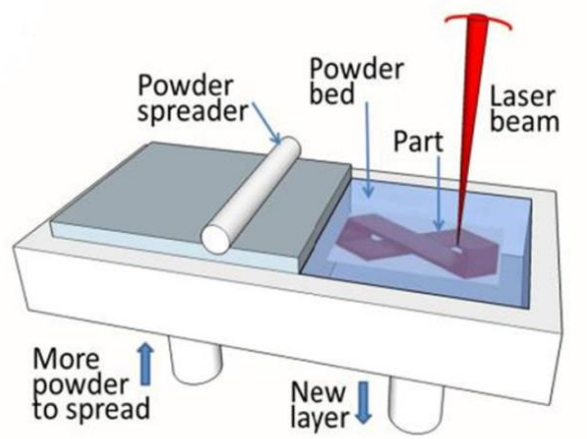


Figure 2.6: Schematic view of the LPBF process [2]

Considering that most of the used laser heat sources adopted in LPBF systems are similar to those of traditional welding processes, information about process-structure-property relationship of interest in the AM of metallic alloys can also be drawn from the welding literature for the same materials.

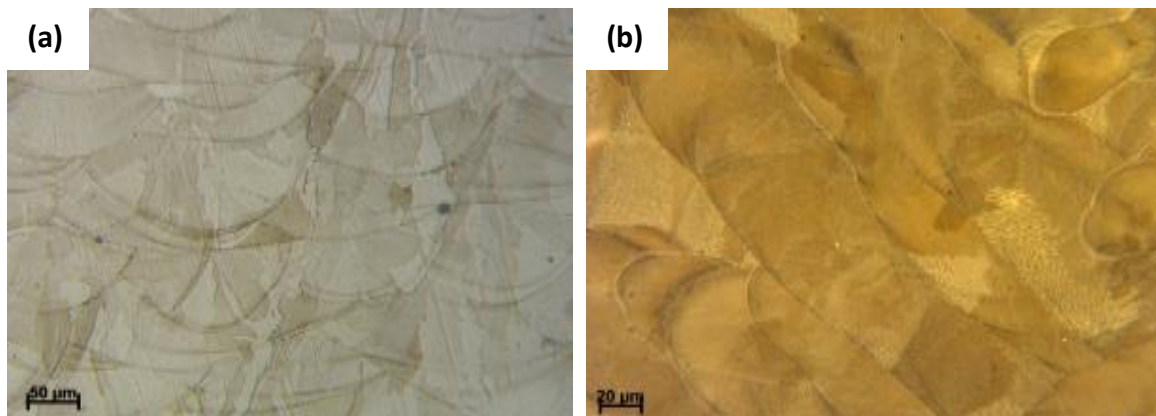


Figure 2.7: Typical microstructure of a LPBF processed alloy, showing laser scan tracks from a lateral view (a) and from upper view (b)

The intrinsic nature of the laser beam and the very fast scanning velocities employed in LPBF process result in very high cooling rates, of the order of 10^6 to 10^8 K/s, which inhibits the grain growth and segregation of alloying elements. Under these conditions the solidification

process starts for each track by epitaxial growth from the substrate of the previously solidified layers and proceeds by competitive growth towards the centre of the melt pool, as shown in figure 2.8. As a result of the competitive grain growth, an almost unidirectional columnar grain structure is often observed during solidification of LPBF process.

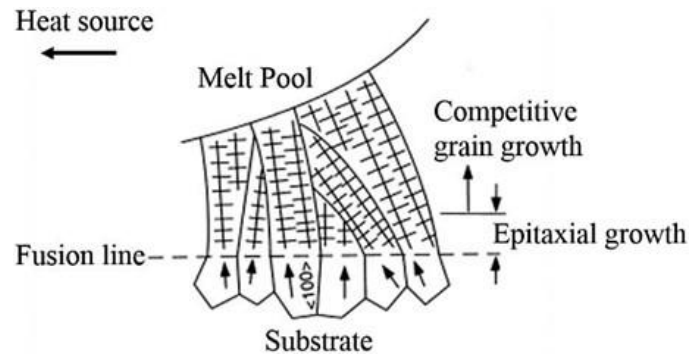


Figure 2.8: Schematic view of the grain growth in LPBF showing the initial epitaxial growth followed by the competitive growth [3]

The key parameters defining the shape of the liquid-solid interface (in terms of planar, cellular, columnar dendritic or equiaxed) are the temperature gradient $G=dT/dx$, the solidification rate $R=dx/dt$, the undercooling ΔT , the diffusion coefficients for solute elements in the liquid D_L .

The size scale of the solidification is usually evaluated in terms of the cooling rate $dT/dt=G \cdot R$. On the other hand, the G/R ratio is responsible for changes in the crystal morphology. By increasing it, the crystal morphology can shift from dendritic to cellular and finally to the planar shape, as depicted schematically in figure 2.9.

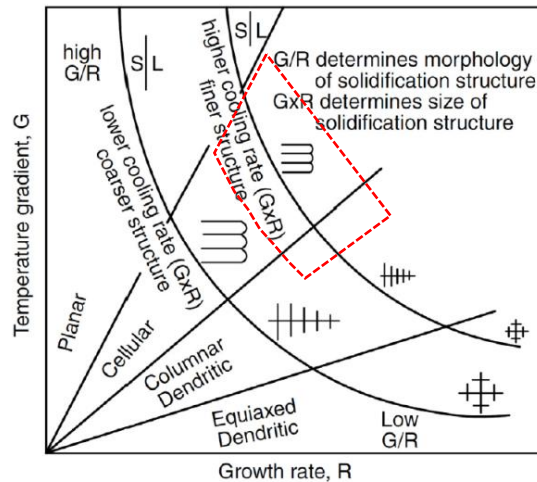


Figure 2.9: The effect of temperature gradient G and solidification rate R on the morphology and the size of LPBF and welding solidification microstructure. The box qualitatively highlights the region covered by LPBF processes [2]

2.3 Literature survey on LPBF of Ni-based superalloys

The following survey has been carried out with the aim of collecting relevant information for the LPBF processing of Ni-based alloys, with particular interest on IN713LC and CM247LC alloys. However, general comments have been collected also considering similar studies describing other AM techniques such as electron beam melting (EBM) and direct metal deposition (DMD) or even laser beam welding (LBW), which share a large variety of common metallurgical concerns with LPBF.

Dilute Ni-based alloys (e.g. IN625 alloy) are considered as readily weldable even though care should be taken to avoid grain boundary cracking in coarse grained materials. On the contrary, more complex precipitation-strengthened alloys (e.g. IN718, and the investigated IN713LC and CM247LC alloys) are more susceptible to welding and LPBF. Defects can be classified in four broad categories [6-8].

- I. *Solidification cracking*: formed in the weld bead when the mushy region (with large fraction of solid - 90%) experiences tensile stresses and the amount of liquid needed to backfill fissures is not enough. Cracking is promoted by wide solidification ranges of the alloys and by low welding speed since the alloy at the sides of the weld starts cooling and generates thermal stresses.

- II. *Grain boundary liquation cracking in HAZ*: forms as a result of local dissolution of low-melting point phases. A liquid film forms in the HAZ which fails under the tensile thermal stresses. Liquation cracking is associated to extensive presence of primary MC-type carbides (NbC, TiC in IN718) or Laves phases; increasing the welding speed increases the cracking susceptibility due to larger stresses and thermal gradients.
- III. *Strain aging cracking*: typically occurs in γ' -Ni₃(Al,Ti) precipitate strengthened alloys due to additional precipitation promoted by post-weld treatments or service at high temperature. Intergranular cracking is promoted either in HAZ and in the WMZ. A similar effect is produced in LPBF by the deposition of each subsequent layer. Strain aging cracking would be limited or healed by the addition of elements that make the precipitation more sluggish (e.g. in alloys strengthened by γ'' -Ni₃(Al,Ti,Nb,Mo) precipitates) and by reducing the amount of elements such as C, B and S that segregate at GBs.
- IV. *Ductility dip cracking*: marked reduction in ductility is found in Ni-based alloys under intermediate temperature conditions (700-900°C for CM247LC alloy). Cracking is caused by the strain concentrations caused by grain boundary sliding that results in void formation typically at triple joints.

A first assessment on the weldability of Ni-based superalloys can be drawn by weldability maps. In these maps the position of each alloy is defined in terms of Al and Ti content in order to evaluate their ability to create dispersion strengthening precipitates. Critical limit lines for processability of alloys are then set as $Ti + Al > 4$ or as $Ti + 2Al > 6$, as reported in figure 2.10.

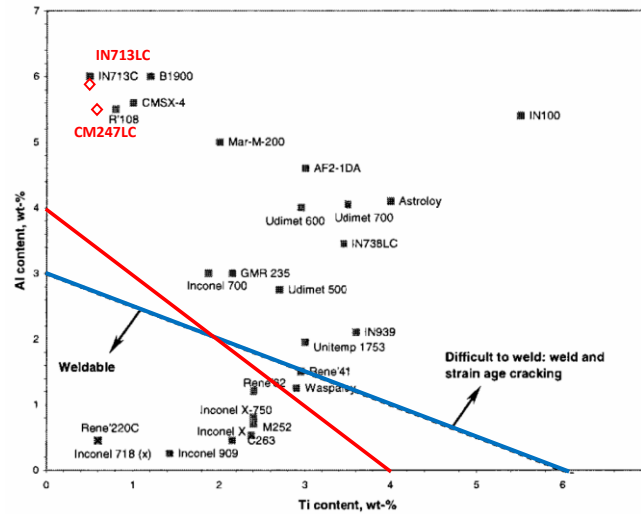


Figure 2.10: Weldability assessment map for a range of Ni-based superalloys, adapted from [6]

Microstructure of IN713LC alloy after thermal treatments

Papers published in [9,10] provide information about the modification of microstructure, as induced by different thermal treatments. An IN713LC cast alloy was investigated in different conditions:

1. as cast state
2. heat treated at 1240°C for 2 hours, followed by water quenching
3. heat treated at 1240°C for 2 hours, followed by air cooling
4. heat treated at 1240°C for 2 hours, followed by furnace down to 940°C, then air cooling

The as cast condition (see figures 2.11a and b) featured extensive segregation with formation of GB phases such as (Nb, Ti)(C, N) (A in the figure), Ni₃Al which forms during solidification (B in the figure) and mixed eutectic constituent rich in Zr (C in figure). In the matrix numerous fine precipitates of the γ' phase are also observed.

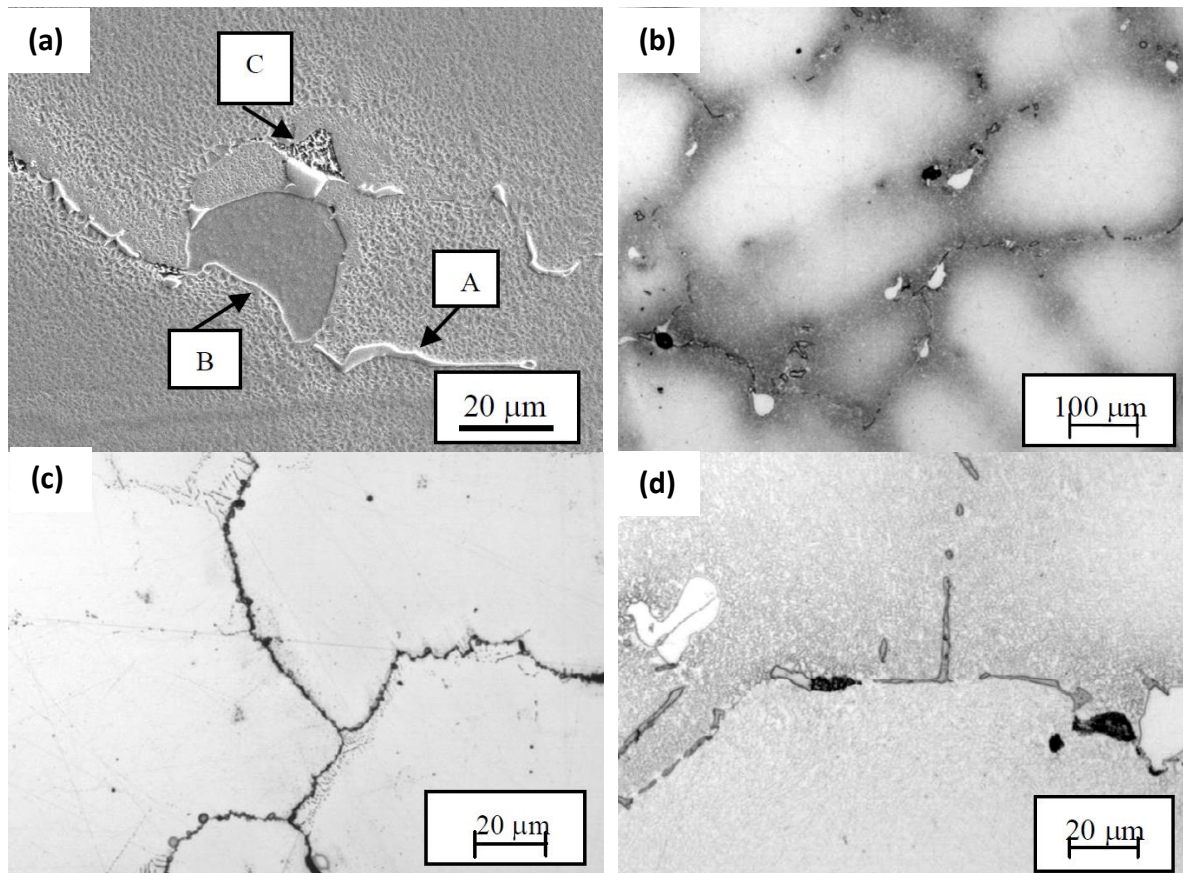


Figure 2.11: Evolution of microstructure in IN713LC alloy after different heat treatments: as cast (a) and (b), heat treatment 2 (c), heat treatment 4 (d) [9].

After heat treatment #2, homogenization of the microstructure became visible, with removal of the segregation evidence. However, frequent interdendritic cracks were observed (figure 2.11 c). Finely dispersed carbonitrides of the type (Nb, Ti)(C, N) were found at GBs. It is believed that the treatment was not able to dissolve these carbides and they promoted cracking due to rapid cooling. Treatment #3 led to a similar microstructure but free from intergranular cracks owing to the slower cooling.

Finally, treatment #4 promoted the re-precipitation of the finely dispersed strengthening phase γ' starting from grain boundaries (figure 2.11 d).

Cracking in electron beam welded IN713LC gas turbine blades

Papers published in [11,12] report about a numerical FEM model developed to study EBW of IN713LC cast alloy on samples cut from the shroud surface of gas turbine engines. Thermal history and residual stress distribution are described.

After welding a significant number of transverse-to-weld cracks were detected in the WMZ and in the HAZ, as depicted in figure 2.12. The estimated cooling rates of the WMZ were in the range of $4 \cdot 10^3$ K/s. A relation between cooling rate and secondary dendrite arm spacing (SDAS) in the microstructure could be defined according to figure 2.13.

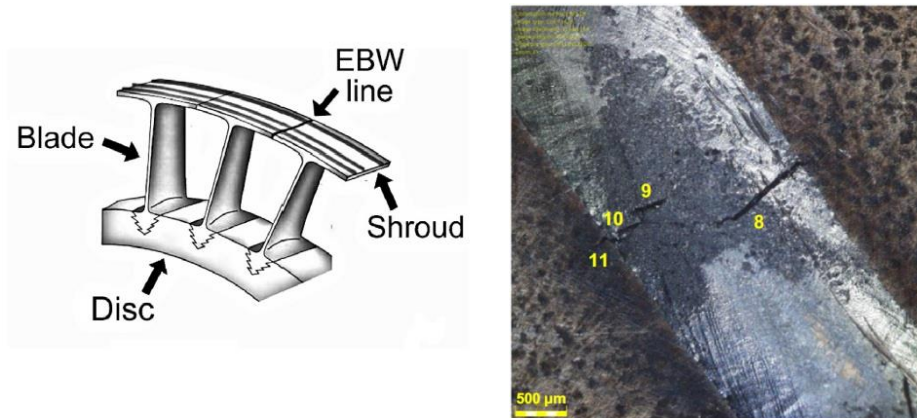


Figure 2.12: View of the weld position and of transverse-to-weld cracks found on samples [11]

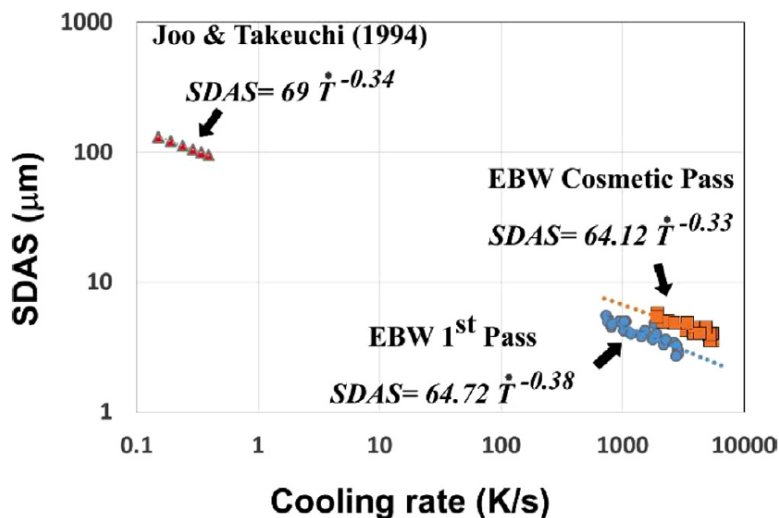


Figure 2.13: Evolution of SDAS as a function of cooling rate during EBW of IN713LC alloy [12]

From the FEM model it is evaluated that longitudinal and transversal residual stresses in WM and HAZ can reach 700-800 MPa. Their distribution follows the trend depicted in figure 2.14. Two types of cracking mechanisms have been detected from analyses. Segregation induced GB liquation (solidification cracking) in WM: EDS analysis qualitatively suggested the segregation of alloying element such as Nb, Si, B, and C in the cracked area. In other sampled area: Mo, Si, Ca, Fe, S, and C were detected. It can be concluded that cracking

took place due to liquation of low-melting constituents with the concurrent action of shrinkage stresses and the low strength of the alloy at high temperature.

Liquation cracking in the HAZ: segregation of alloying elements such as Mo, Zr, Nb, S, C, and B in the cracked area of HAZ was observed. Sulfides, sulfocarbides and M_3B_2 borides are problematic during fusion welding because of their low melting point (1245°C and 1140°C, respectively), especially when they form liquid films at GBs.

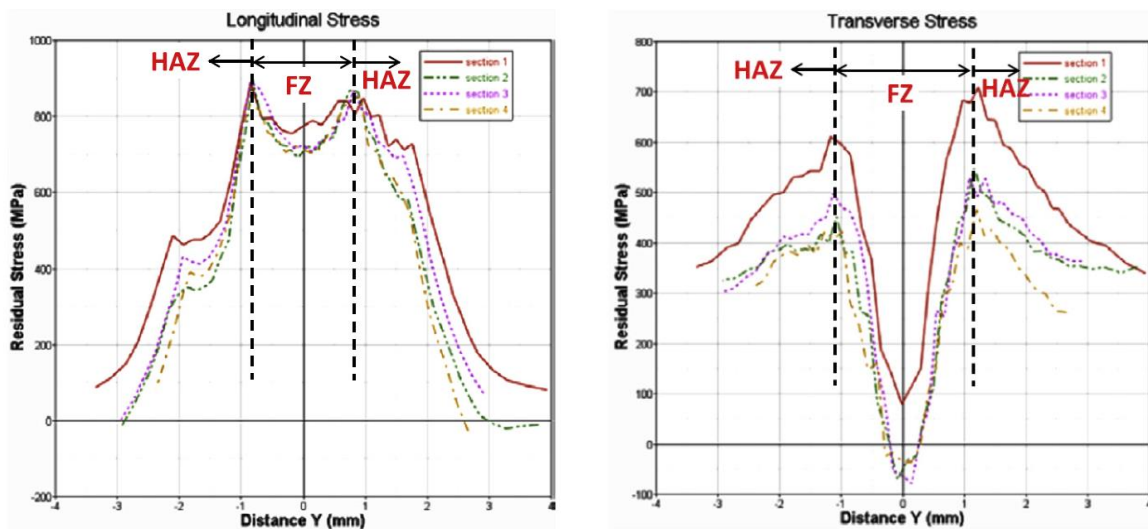


Figure 2.14: Longitudinal and transverse residual stresses (in Y-direction, along weld bead) in the investigated samples [11]

Thermophysical properties of IN713LC alloy

Accurate thermal analyses described in [13] supply useful data about transformation temperatures of an investment cast IN713LC alloy.

A representative Differential Thermal Analysis (DTA) curve collected on cooling from the liquid phase is depicted in figure 2.15 while table 2.3 summarizes the main transformation temperatures as a function of the applied cooling rate. The phase transformations found on solidification are:

- melting $\rightarrow \gamma$ phase
- melting $\rightarrow \gamma + MC$
- melting \rightarrow eutectics γ/γ'
- melting $\rightarrow \gamma +$ minority phases (e.g. borides)
- matrix $\gamma \rightarrow \gamma'$

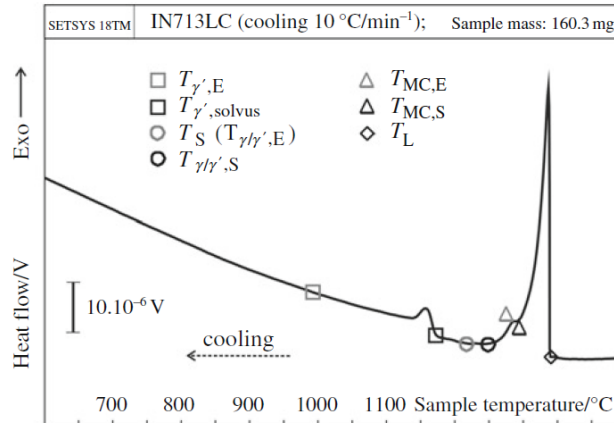


Figure 2.15: DTA curve of the IN713LC alloy (cooling rate 10°C/min) [13]

Table 2.3: Transformation temperatures of the IN713LC alloy for various cooling rates, as determined by DTA [13]

Cooling rate/°C min ⁻¹	Temperature of phase transformation/°C						
	T_L	$T_{MC,S}$	$T_{MC,E}$	$T_{\gamma/\gamma',S}$	$T_S (T_{\gamma/\gamma',E})$	$T_{\gamma',solvus}$	$T_{\gamma',E}$
50	1324	1262	1249	1223	1193	1183	925
20	1329	1283	1270	1238	1213	1182	953
10	1338	1289	1286	1238	1219	1175	996
5	1339	1294	1290	1251	1227	1178	1084
1	1346	1341	1295	1262	1233	1167	1114
0 (calc.)	1343	1314	1294	1254	1230	1172	1074
5 [15]	1356	1312	1304	1278			
5 [16]	1355	1315		1281			

From results it can be assumed that in the range of dissolution of the γ' phase, the dissolution of other minor phases may occur (e.g. phases η (Ni_3Ti) or borides M_3B_2). The broad melting peak observed in the DTA thermograms, also comprises several transformations, which follow closely one after another (γ/γ' eutectic and MC type carbides dissolution).

From table 2.3 it is shown that the temperatures of transformation decrease with increasing cooling rate. However, the solidification range obtained at the rates 1–20°C/min was almost identical. Contrarily, the broadest interval of precipitation of γ' was observed at 50°C/min (258°C) while the narrowest range (53°C) was observed at the rate of 1°C/min.

Representative micrographs collected after cooling at 20 and 50°C/min are given in figure 2.16.

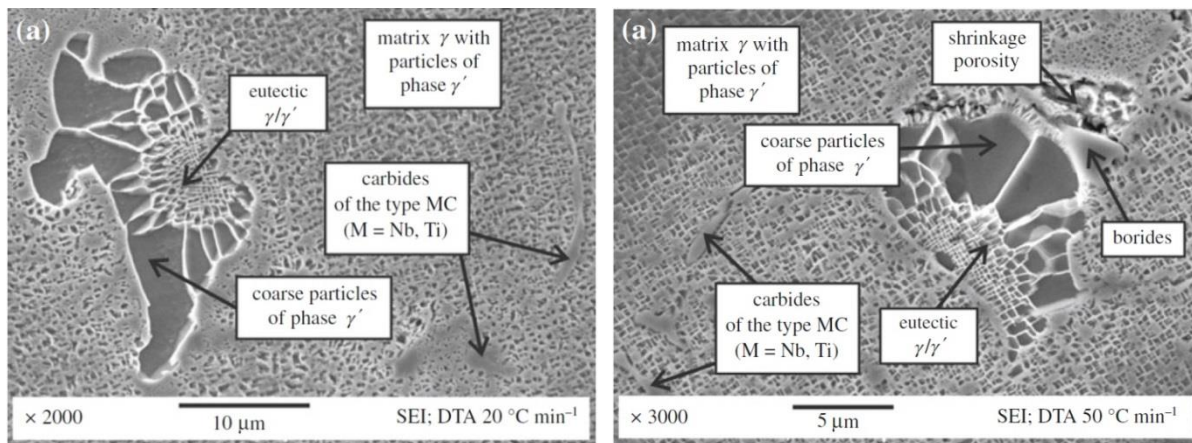


Figure 2.16: SEM micrographs of IN713LC alloy, cooling rate 20 C/min (a) and 50 C/min (b) [13]

Influence of processing parameters on LPBF of CM247LC alloy

Carter and co-authors [8] conducted an analysis on defects produced by LPBF processing of a CM247 LC alloy. Details of process parameters are not given as absolute values, but samples are classified according to: high-energy (HE), low-energy (LE), very-low-energy (VLE) conditions (see paper for more details about the relative values of process parameters).

- I. HE conditions mainly produced a «jagged» cracking morphology with evidence of protruding dendrite branches seen at high magnification (solidification cracks).
- II. LE conditions led to more directional cracks aligned almost exclusively in the build direction (direction of grain elongation). Structurally, they appear to be much cleaner and straighter, suggesting that the cracks were formed during the solid state at GBs, corresponding to Strain Aging Cracking or Ductility Dip Cracking.
- III. VLE conditions represented the failure of the process to fully consolidate the powder. The micrographs showed voids with evidence of unmelted powder particles.

Representative images of the defects described are collected in figure 2.17.

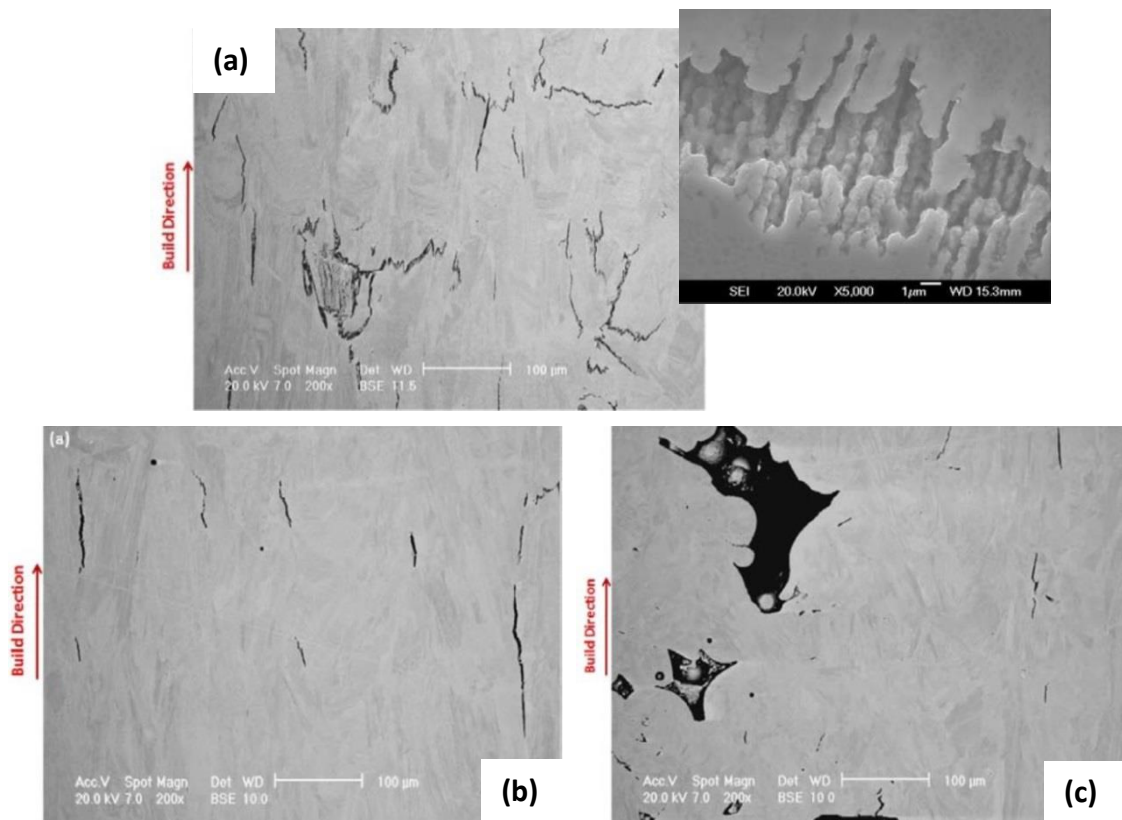


Figure 2.17: micrographs showing defects details found in LPBF-processed samples according to different parameters;
(a) High energy, (b) low energy, (c) very low energy [8]

A drop in cracking level was detected at fairly high scan speed (around 2v or 2.5v, as shown in figure 2.18) when using constant laser power (3 different levels were investigated). This drop in recorded cracking levels corresponded to a change in the dominant cracking type, from solidification cracking for high energies to grain-boundary cracking for low energies. As for the elimination of porosity in the VLE regime, it is suggested that reducing the scan spacing could eliminate porosity, while keeping the number of cracks to a very limited level.

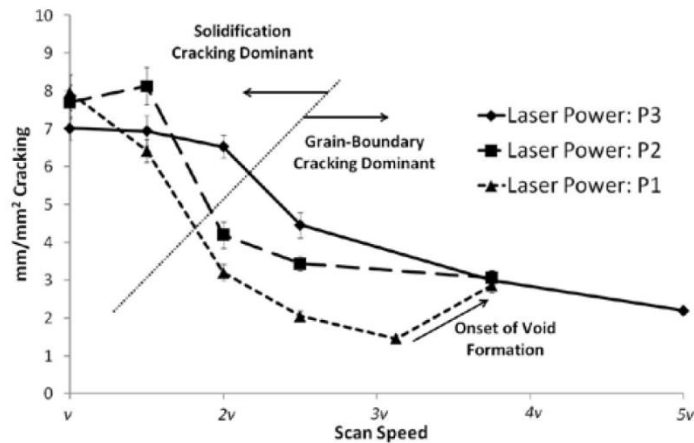


Figure 2.18: Variation of cracking with laser scan speed and LASER power in CM247LC LPBF alloy [8]

In a second paper, the same research group presented results about the influence of laser scan strategy on grain structure and cracking behaviour [14]. Two distinct strategies were considered: Island scan strategy (also called chessboard strategy in the literature) and simple linear scan strategy, as depicted in figure 2.19.

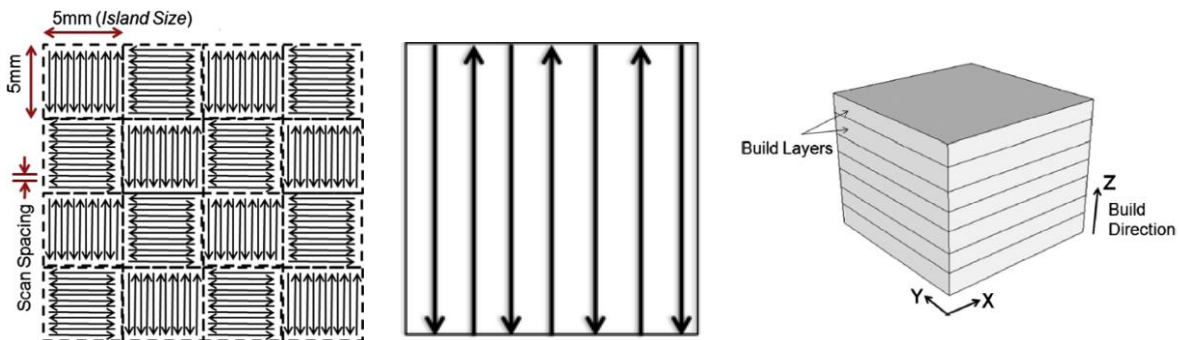


Figure 2.19: schematic representations of the island scan strategy (a), the linear scan strategy (b) and definition of the reference axes and plans of the built samples [14]

Island scanning produced a very distinctive “diamond” pattern with a bimodal grain structure made by large columnar grains (preferred {001} orientation along z axis), as typically found in laser solidified alloys, and a fine-grained region between the columnar grains. It was suggested that the fine-grained regions are caused by the effect of the edges of the ‘islands’ whereas the elongated grains in the build direction always lie in the middle of an ‘island’. Microcracks preferably formed in the fine-grained region due to large crystal misorientation and higher cooling rates.

Effect of heat treatments on microstructure of a CM247LC LPBF-processed alloy

Due to very high cooling rate encountered during the LPBF solidification, post-process heat treatments are necessary to develop γ' precipitates to the desired size in most Ni-based superalloys. In a research work by Divya et al. [15], it is recalled that the as-deposited state of most of the precipitate-strengthened Ni-base alloys is made up of fine cells with limited precipitation of γ' and γ'' , as well as a high density of dislocations at cell boundaries, as shown in figure 2.20.

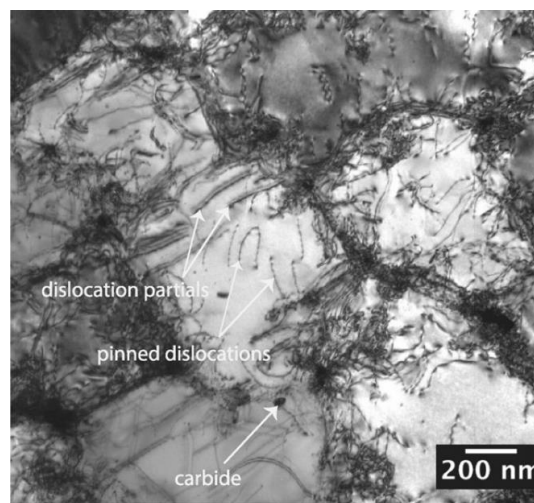


Figure 2.20: Bright field TEM image of a transverse section of the as-built CM247 specimen showing the cell structure [15]

In the investigation, two distinct conditions for the LPBF materials were considered together with a reference CM247 alloy produced by conventional casting:

- as built by LPBF
- as built, thermally treated at 1230°C for 2h followed by air cooling
- As cast, thermally treated at 1260°C for 18h followed by air cooling and further holding at 870°C for 18 h followed by furnace cooling

DSC thermograms highlighted the temperatures of γ' dissolution, of carbide dissolution and of the solidification interval for the 3 conditions, as reported in table 2.4.

Table 2.4: Phase transition temperatures of the materials investigated obtained from DSC on heating and from predictions using Thermo-calc [11]

Phase transformation	DSC measurements		
	as-SLM	SLM + HT	CC
$\Delta T_{\gamma'} = T_{\gamma' \text{ start}} - T_{\gamma' \text{ end}}$	1254–1265	1246–1265	1239–1252
Solidus, T_s	1279	1279	1295
Carbide dissolution, T_c	1357	1356	1355
Liquidus, T_L	1373	1373	1373

Phase transformation	ThermoCalc-predictions	
	TCNI5	TTNI8
$\Delta T_{\gamma'} = T_{\gamma' \text{ start}} - T_{\gamma' \text{ end}}$	1257	1209
Solidus, T_s	1257	1297
Carbide dissolution, T_c	1293	1358
Liquidus, T_L	1385	1372

The observed microstructure (see figure 2.21) was composed of elongated columnar grains along the build direction, crossing multiple deposited layers. In the transverse direction, a bimodal distribution of grains was observed. EBSD maps indicate that the post LPBF heat treatment reduced the texture and caused limited, localised recrystallization.

Cracks (and gas porosity) were observed. Cracking was more pronounced at edges of specimens than in the bulk. They featured both intergranular and intragranular growth modes, as shown in figure 2.22.

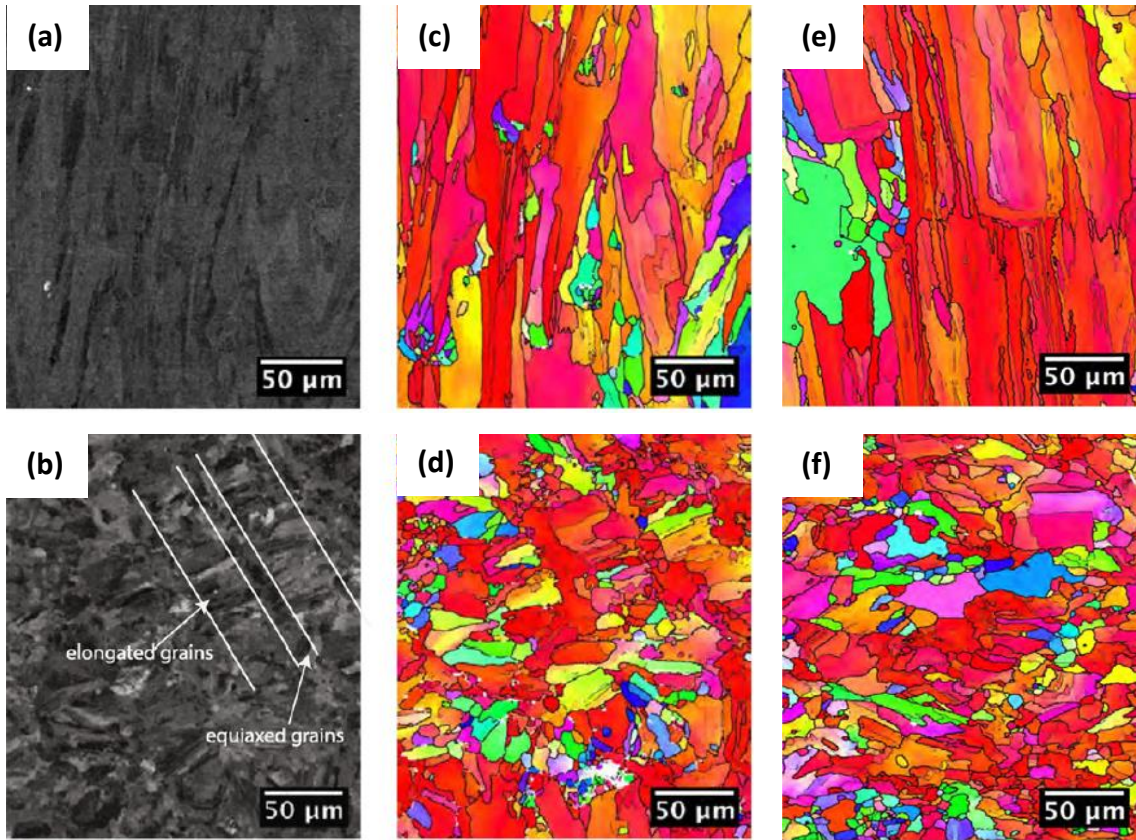


Figure 2.21: SEM images of the CM247 LC alloy (longitudinal view along build direction on top line, transverse view on bottom line); BSE micrographs of as built samples (a and b), EBSD maps of as built samples (c and d), EBSD of heat treated samples (e and f) [15]

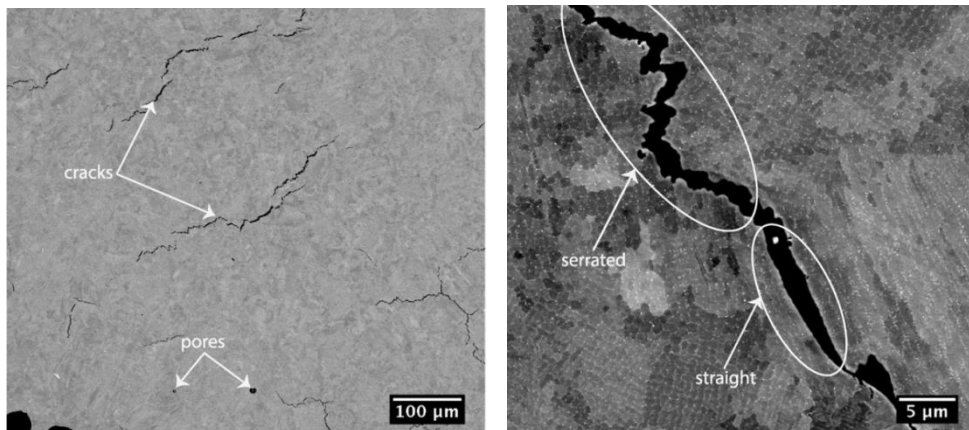


Figure 2.22: SEM micrographs of cracking detected in samples [15]

EBM of γ' precipitation-strengthened Ni-based superalloy

DZ125 is the commercial name of a Chinese γ' precipitation-strengthened Ni-base superalloy that is similar to Rene142 and CM247LC in terms of Al, Ti and Hf contents. The paper in [16] deals with electron beam melting (EBM) processability of the DZ125 alloy.

In contrast to LPBF, in EBM the electron beam works under vacuum conditions, it can be moved at extremely high velocities and can deliver a high-power input. As a result, the consolidated material can be tuned in order to solidify by fine or coarse-grains, texture-free or highly-textured.

The investigation showed that the as EBM microstructure consisted of columnar grains with varying size (depending on processing conditions) with aligned Hf-rich MC-type carbides at their boundaries, as shown in figure 2.23. Smaller γ' precipitates were found at dendrite cores.

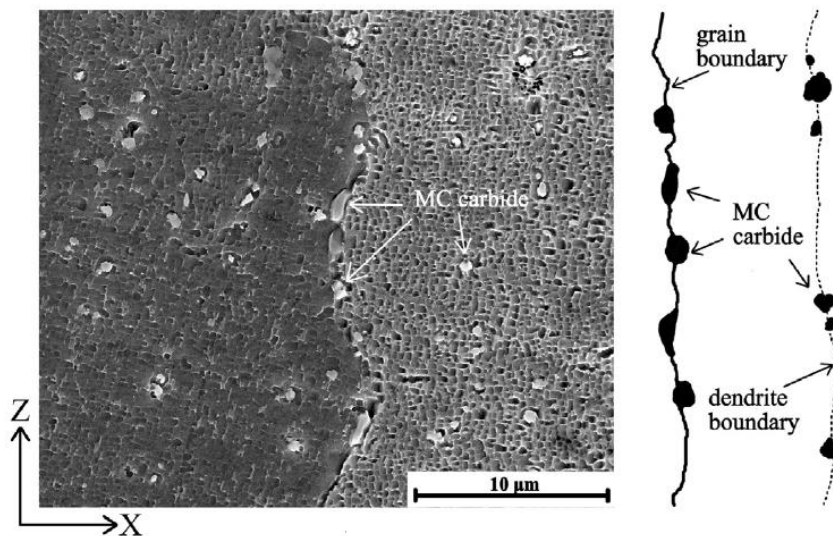


Figure 2.23: SEM micrograph of as-EBM sample showing the distribution of MC carbides preferably at the columnar grain boundaries and dendrite boundary regions [16]

Cracks primarily parallel to build direction were found for both coarse columnar grained and fine columnar grained samples in as-EBM condition. These cracks are only formed at columnar GBs that were decorated with MC carbides but not along carbide-free dendrite boundaries.

Cracking, which is classified as solidification or liquation cracking, is attributed not only to MC carbides but also to the degree of GB misorientation.

Chauvet and co-workers also published investigations on EBM of a non-weldable Ni-based superalloy [17,18]. The alloy is only described as Ni-Co-Cr-Mo-Al-Ti-B superalloy containing significant amounts of Cr, Co and Mo and with Ti + Al = 8,6 wt.%.

Samples were processed by EBM, preheating the powder bed by defocused beam passes to around 1050°C before being selectively melted. Tuning the beam properties and selecting the scanning strategy allowed achieving a progressive grain selection during solidification ending up with few highly texturized coarse columnar grains on top of the build, as depicted in figure 2.24.

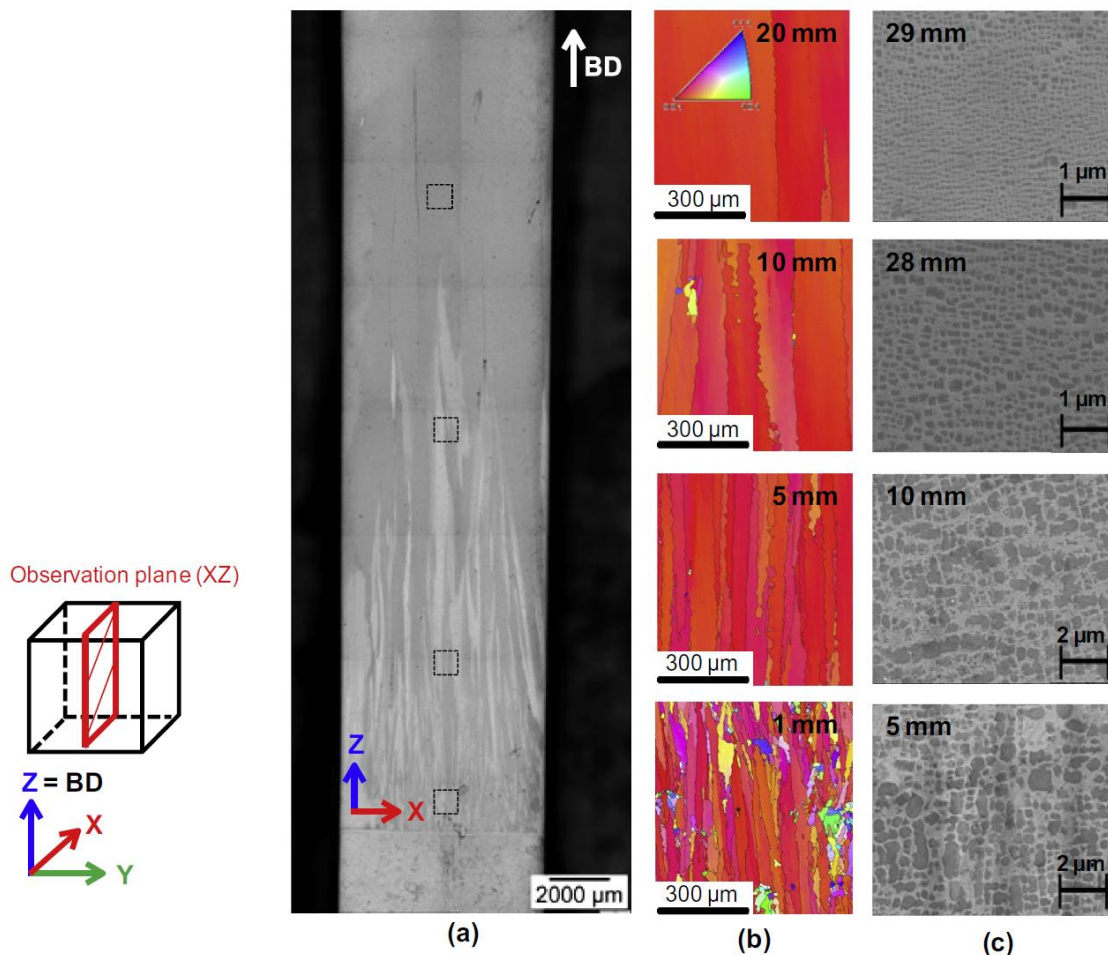


Figure 2.24: Microstructure of as-built specimens observed in the central part on a XZ cross section. (a) Optical micrograph showing the macrostructure, (b) EBSD maps showing the columnar grain size evolution and (c) BSE-SEM micrographs illustrating the size of the γ' precipitates at different positions along the build direction [18].

Moving along the build direction (z) produced a shift from fine randomly oriented grains with high-angle grain boundaries (HAGBs) into coarse mm-size grains separated by Low-

angle grain boundaries (LAGBs). The GB density also decreased while the size of γ' precipitates only slightly decreased.

Well-aligned chains of rounded pores were found along the columnar grain growth direction with a typical diameter lower than 5 μm . They are believed to form during the last stages of solidification, when bridging occurs between dendritic secondary arms (microshrinkage).

Cracks running intergranularly along the build direction over several millimetres were also detected (see figure 2.25). Cracks were only observed when the columnar grain width was larger than approximately 150 μm and their misorientation corresponded to HAGBs. Boundaries of cracked grains were decorated with borides that were identified by atom probe micrography (APT) as MB, M_2B and M_5B_3 . All three types of borides were observed to be Mo- and Cr-rich.

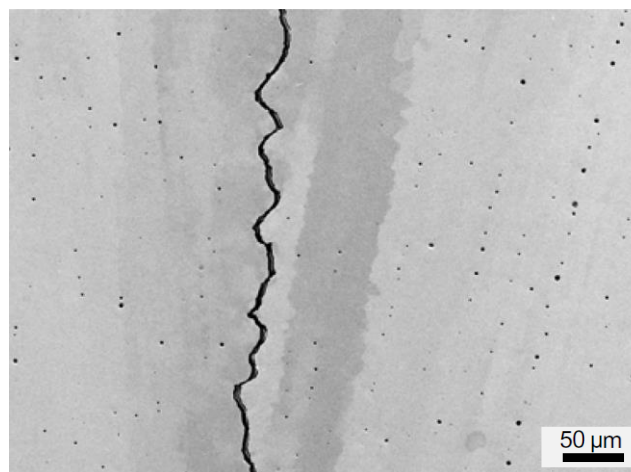


Figure 2.25: SE-SEM micrograph illustrating a crack running along the build direction and intragranular well-aligned rounded-shape pores [18]

From fracture analysis the authors were able to show that cracking most likely must have occurred when a liquid film was wetting the dendrites during the last stage of solidification. Namely in the range when the fraction of solid changes from about 0.95 (coalescence fraction) to 1, the so called “critical temperature range”.

In situ heat treatment of Inconel 718 during EBM

The work presented in [19] is a first attempt to achieve an a-priori designed microstructure by EBM, with modified beam control to rule the temperature holding and the cool down conditions from the processing temperature. These In situ heat treatments (ISHT) have been

tested on an IN718 alloy powder. Cool down rate after build completion was controlled by the build chamber atmosphere: vacuum brings a cooling rate of 0,07-0,08 K/s, helium injection produces a cooling rate of 0,1-0,2 K/s. the EB power was used to heat continuously the powder bed (even though excessive over-sintering of powder was obtained).

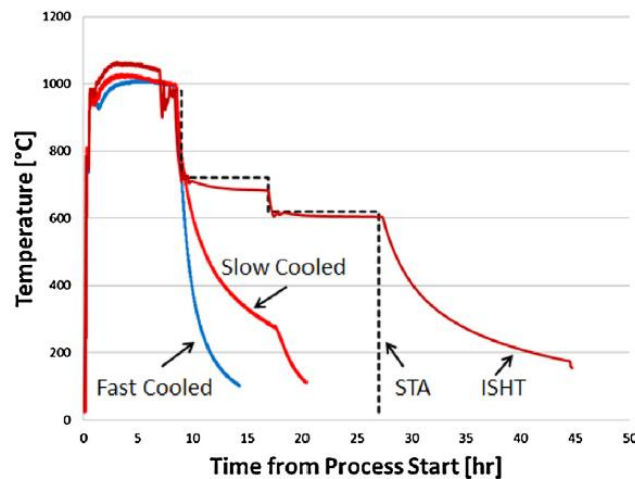


Figure 2.26: Thermal histories as measured from start plate thermocouple for various cool down techniques. The standard heat treatment (STA) is plotted for comparison to the ISHT [19].

As reported in figure 2.26, by appropriate tuning of the processing parameters, the target thermal cycles could be obtained. Precipitation of both γ'' and γ' was achieved, leading to hardness values comparable to those of wrought IN718 alloy. However, mechanical properties were quite poor due to a combination of unusually large grain size and cracking.

Understanding the heat flow thermal cycles of AM materials

The research group led by T. DeBroy at Pennsylvania State University already in 2014 developed a 3D, transient, heat transfer, and fluid flow model for the laser assisted multilayer direct metal deposition (DMD) process with coaxially fed powder, as described in [20]. Although the process differs from LPBF for some aspects, general information and trends can be derived from their model output.

It is firstly considered that the solidified material undergoes multiple heating and cooling cycles as new layers of the alloy are deposited on the previously deposited layers. The thermal model accounts for these effects by solving equations of conservation of mass,

momentum, and energy with appropriate boundary conditions and temperature dependent properties of materials in different regions of the system (see figure 2.27 and 2.28).

The main output of the model are the temperature and velocity fields, cooling rates, and solidification parameters.

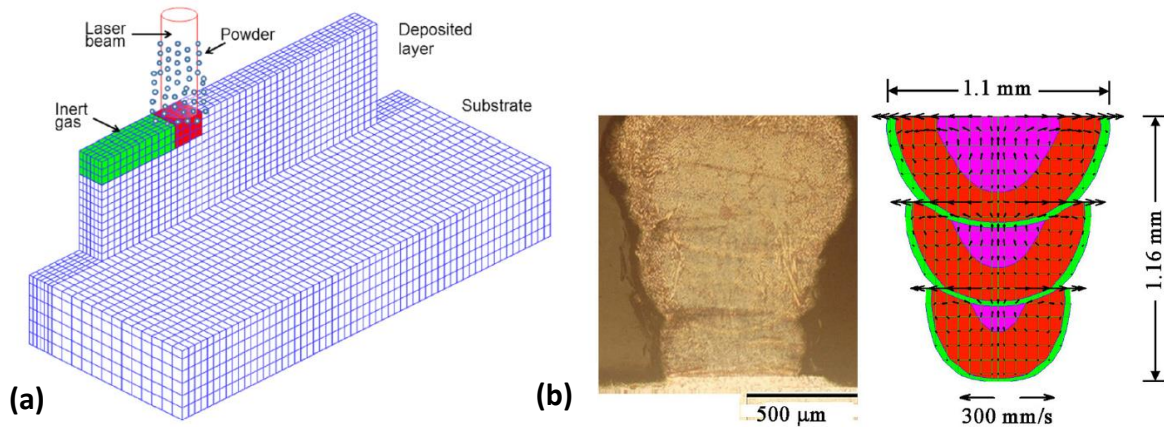


Figure 2.27: Schematic representation of the solution domain for the model (a) and comparison of the experimental and predicted shape of a three-layer deposit (b) [20]

The computed thermal cycles for a three-layer 316 stainless steel sample produced by DMD are shown in figure 2.28 for three reference positions, each taken at mid-length and mid-height within the first, second and third layer. The trend highlights the complex thermal cycles felt by the additively deposited material. Each thermal cycle shows the expected recurrent spikes. The thermal cycles are indicative of the progress of layers deposition during the process.

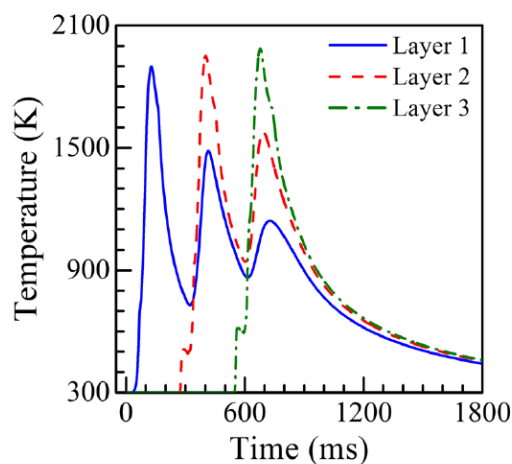


Figure 2.28: Thermal cycles at three locations in the first three deposited layers of a 316 stainless steel sample [20]

The model was further applied to the multi-layer printing of an IN718 alloy for the development of the grain structure during solidification [21]. Also for this more complex configuration, a similar trend of the thermal cycles was highlighted, as illustrated in figure 2.29.

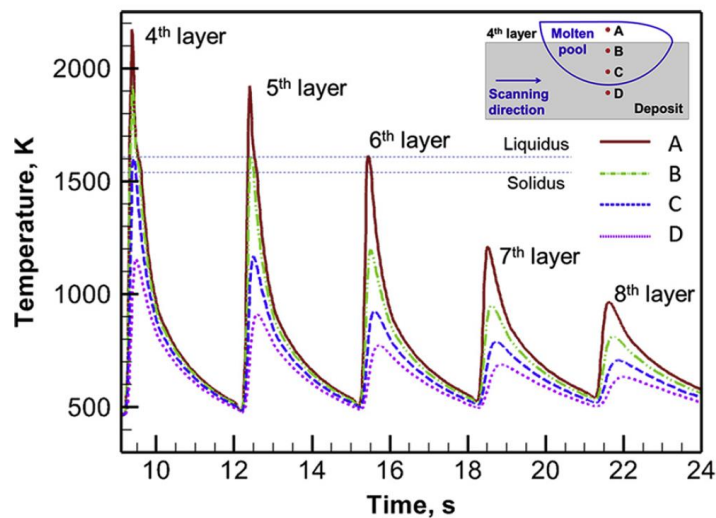


Figure 2.29: Thermal cycles at different monitoring locations during DMD of a multilayer deposit of In718 alloy [21]

It is then to consider that the translation of similar trends to LPBF processing would show the overlapping effects of the tracks deposited side by side on the same layer and those brought by the deposition of subsequent layers. In very recent times, models were improved to account for these additional features. Thermal models have been published to show the effects of lateral tracks in single-layer deposits simulating the LPBF process [22,23]. When defining the physical properties of the materials, the models take into account that the loose powder has a heat conductivity which is approximately hundred times smaller than the consolidated solid material. Therefore, coefficients are implemented in models accounting for these differences, reducing the thermal properties to fixed values or relating them to the amount of void fraction found in the powder bed [24].

Figure 2.30 summarizes some results published in [23] about the thermal field produced on a powder bed during laser scanning of an Al-Si10-Mg alloy. Even though the alloy differs from those investigated in the present project, there is qualitative evidence about the pre-heating effect produced by the laser track on the bed area still to be scanned (figure 2.30a) and on the different thermal gradients found laterally to the molten pool given by the distinct

thermal properties of the solid material and of the powder bed (on right and left side of the molten pool in figure 2.30b, respectively).

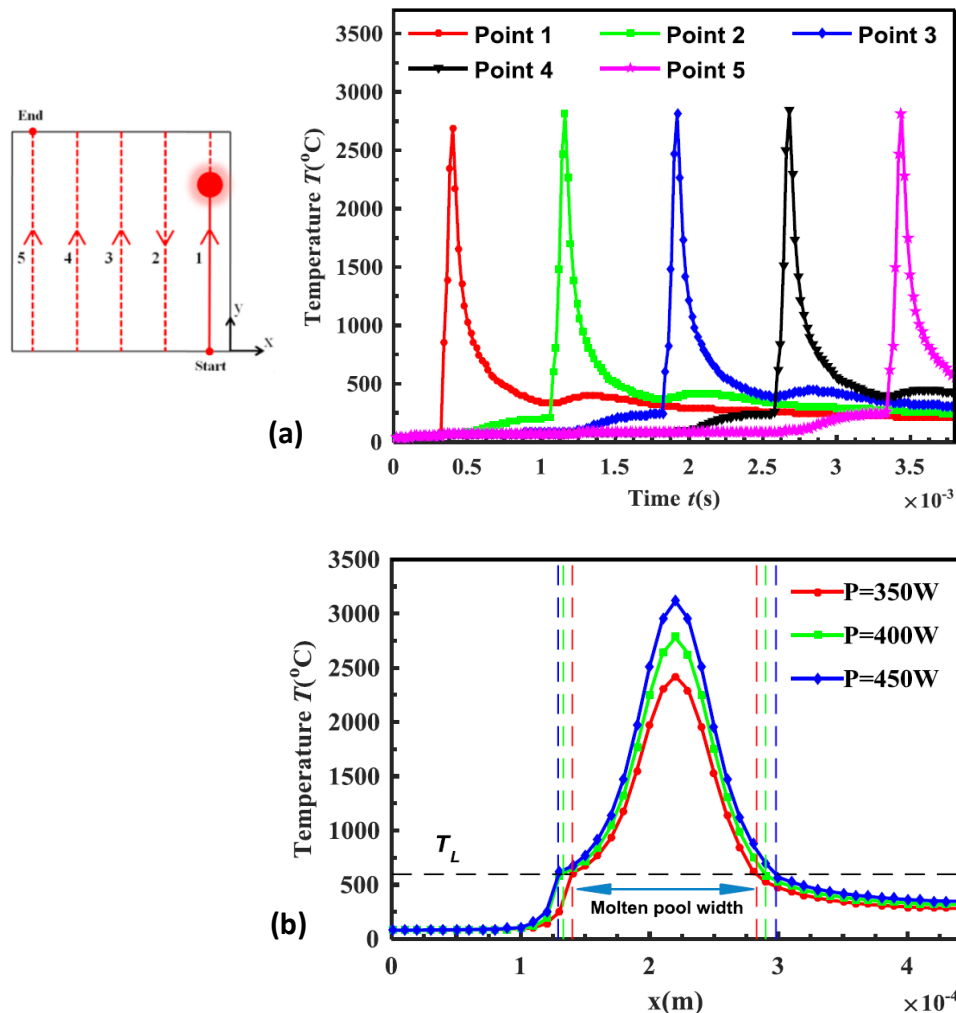


Figure 2.30: Temperature distribution at center of each scanning track (a) and transversally to second track (b) in a LPBF deposited Al alloy [23]

Multi-layer scan patterns have also been implemented in models recently [25-28]. Additional points to be considered for such configuration are not only the property changes during phase transitions (from powder to liquid to vapor to solid) but also the modification of the volume occupied by the deposited material during the different processing stages. Figure 2.31 clearly illustrates these expected changes for a multi-pass LPBF process [25].

3D models can therefore capture the temperature distribution, residual stress field and distortion pattern of LPBF parts with reasonable accuracy. A typical output from such models is provided in figure 2.32 and 2.33 for a multiple-track, four-layer scan on a square surface of

a 316 stainless steel [25]. The thermal history produced on bottom of a single layer substantially reflects the already mentioned effects of the repeated scans (figure 2.32 a and b) while the 3D temperature profiles at fourth layer deposition are indicative of the heat flow toward the underlying material (figure 2.33).

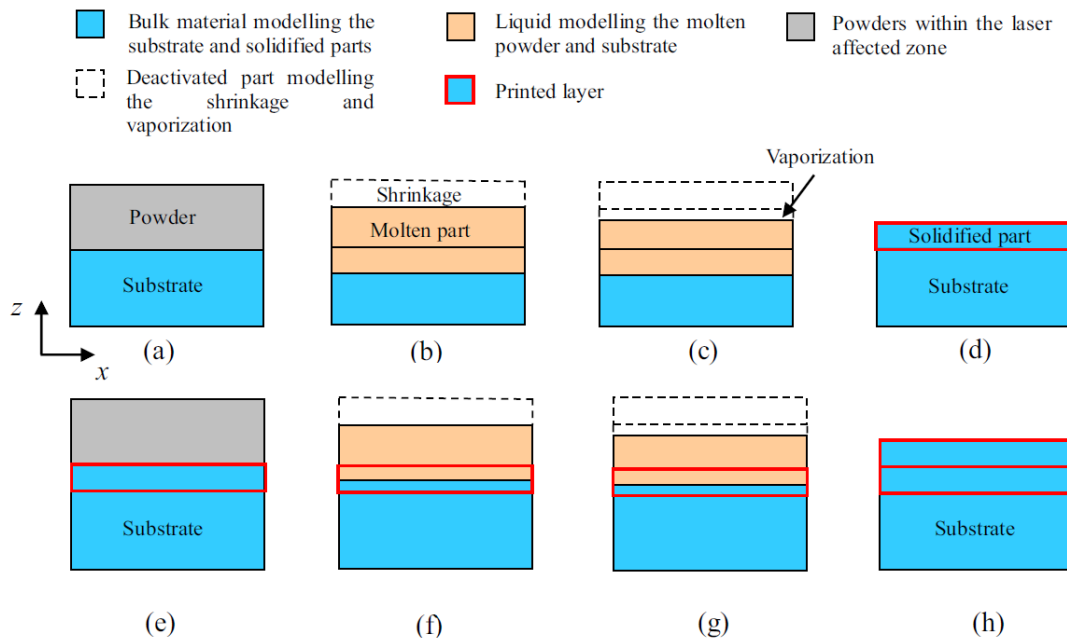


Figure 2.31: The multi-layer modeling of the LPBF process. The cross sections of one-layer is shown from (a) to (d), after the molten material cools down, a new layer of powders is spread and the processes in (e) – (h) [25]

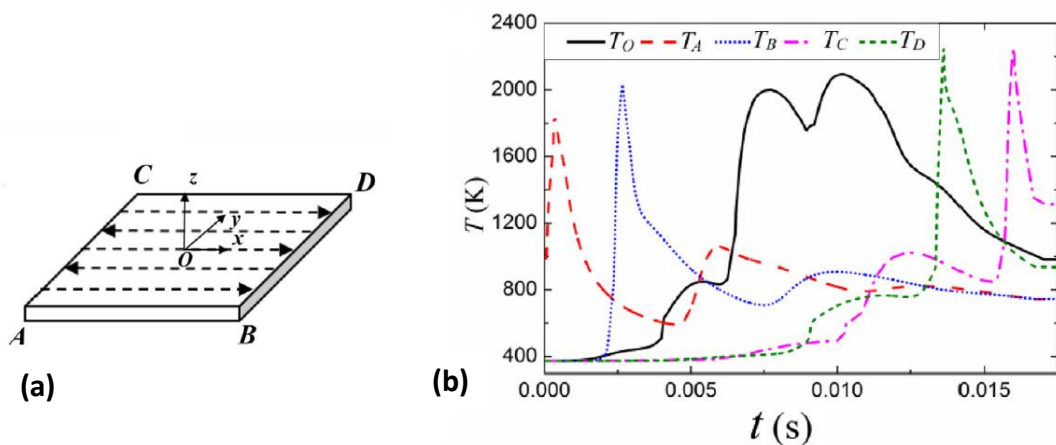


Figure 2.32: Scan track pattern on a single layer (a) and temperature profiles at different locations (b) [25]

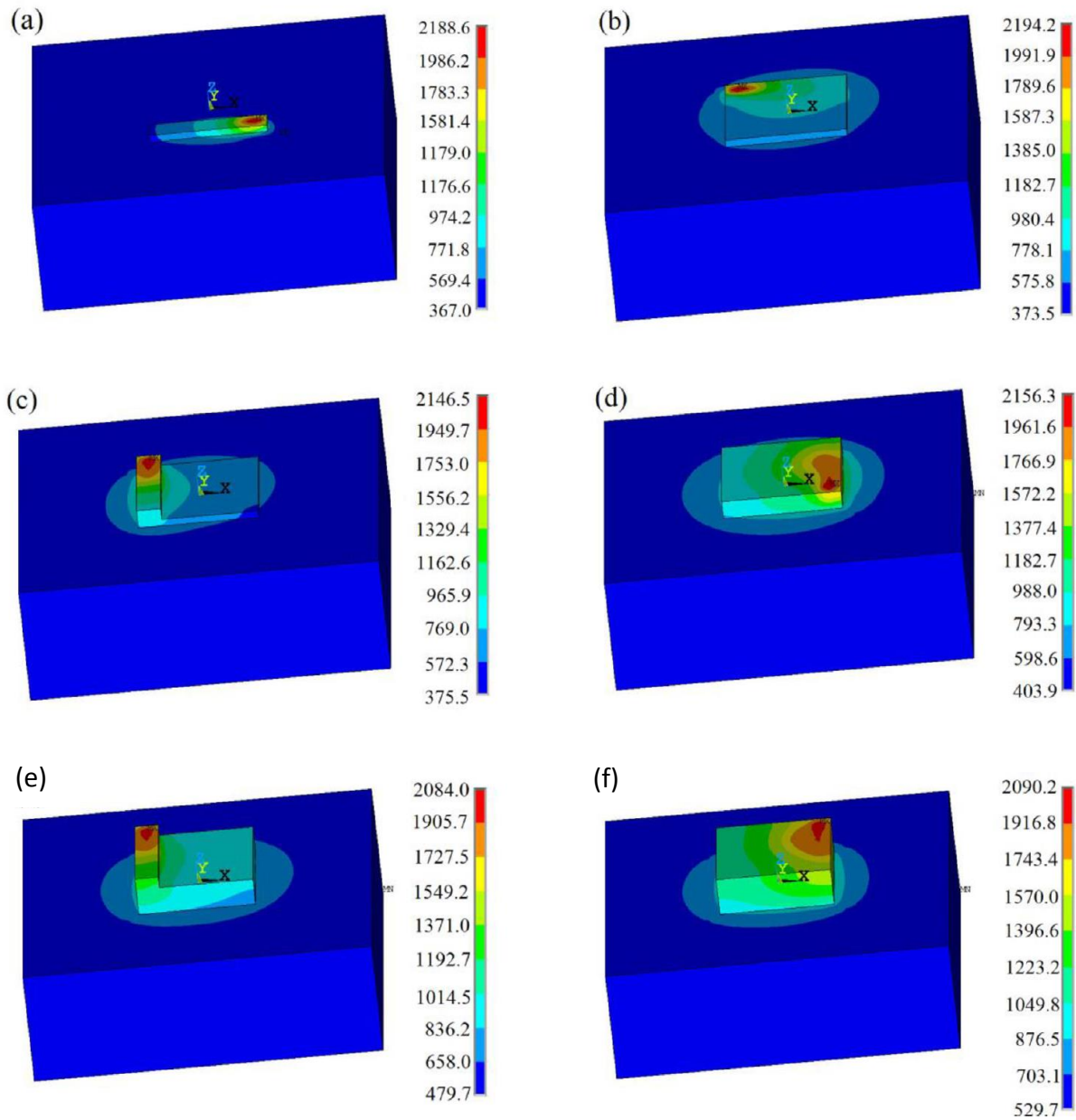


Figure 2.33: Temperature profiles in the first layer(a, b) second layer (c,d) and in the fourth layer (e, f) with bidirectional scanning strategy during LPBF of a 316 stainless steel [25]

3 AUSTENITIC STAINLESS STEELS AND LASER BEAM WELDING

3.1 Austenitic stainless steels and their weldability

Austenitic stainless steels (SS) are widely used in a large number of industrial fields due to their mechanical strength and ductility, corrosion resistance and high-temperature creep properties. They are generally considered as weldable if proper precautions are followed [29].

The stability of the microstructure is primarily affected by their chemical composition, as dictated by constitutional diagrams such as the Sheaffler diagram (figure 3.1a) or more recent evolutions of it (figure 3.1b).

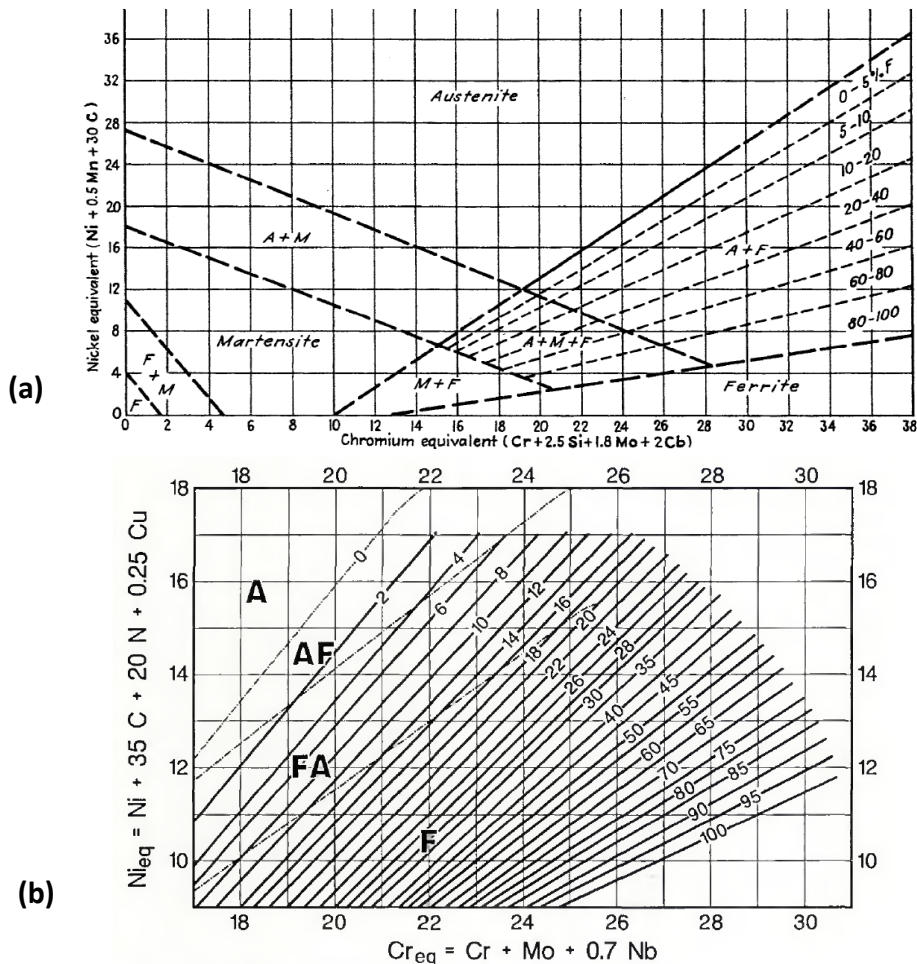


Figure 3.1: constitutional diagrams for stainless steels; Shaeffler diagram (a) and WRC-1992 diagram (b) [29]

The chemical compositions of the two most popular SS grades, which will be mainly considered for the following literature survey, are reported in table 3.1.

Table 3.1: Nominal chemical composition (wt.%) and mechanical properties of three austenitic stainless steel grades [29]

grade	C	Mn	P	S	Si	Cr	Ni	Mo	Fe	UTS (MPa)	YS (MPa)	F.E. (%)
304	0,08	2,0	0,04 5	0,03	1,0	18,0 – 20,0	8,0 – 10,5	-	bal.	515	205	40
304L	0,03	2,0	0,04 5	0,03	1,0	18,0 – 20,0	8,0 – 12,0	-	bal.	480	170	40
316	0,08	2,0	0,04 5	0,03	1,0	16,0 – 18,0	10,0 – 14,0	2,0 – 3,0	bal.	515	205	40

The solidification behaviour of austenitic SS can be described by the use of pseudo-binary Fe-Cr-Ni diagrams at 70% Fe (see figure 3.2), evaluating the contribution of other elements in terms of Cr_{eq} and Ni_{eq} , it is observed that primary solidification can occur either as austenite or as ferrite. The nominal compositional range (from heat to heat) of many austenitic SS is broad enough that both modes are possible.

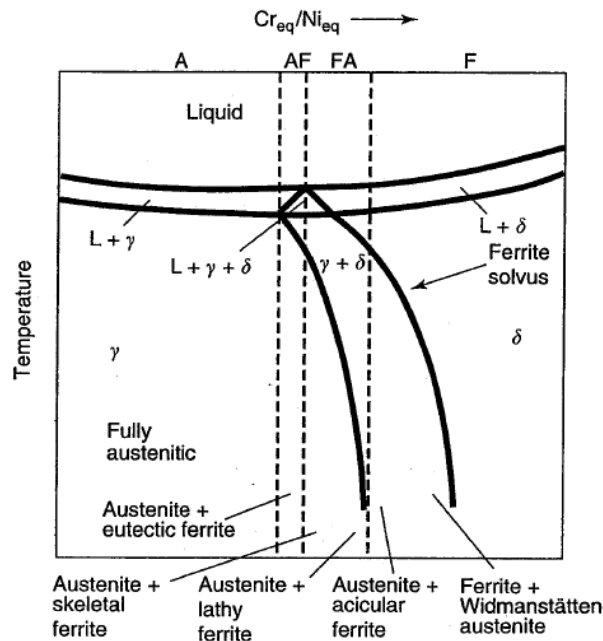


Figure 3.2: Fe-Cr-Ni Pseudo-binary phase diagram at 70% Fe showing the different solidification modes for austenitic SS [29]

As a result of the rapid cooling and partial solid-state transformations, a residual amount of ferrite can be found in most austenitic SS. Precipitation of secondary phases is also frequent. Especially, $M_{23}C_6$ carbides form very rapidly along GBs in the temperature range 700-900°C, as shown in the precipitation-time-temperature (PTT) diagram given in figure 3.3.

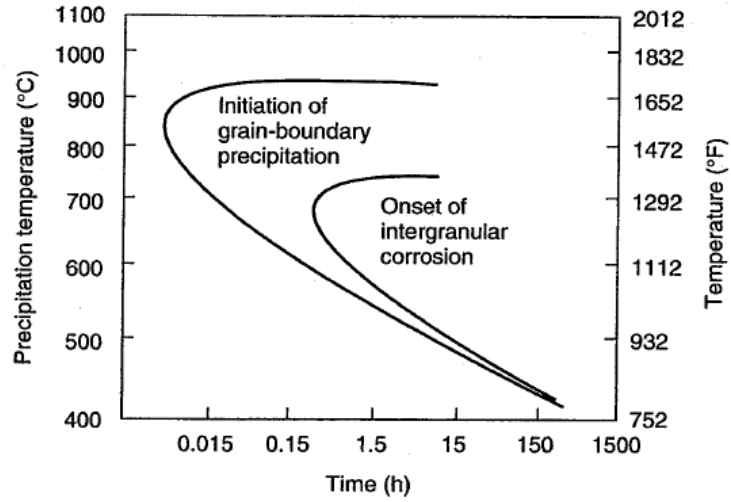


Figure 3.3: Precipitation time-temperature diagram for the 304 SS [29]

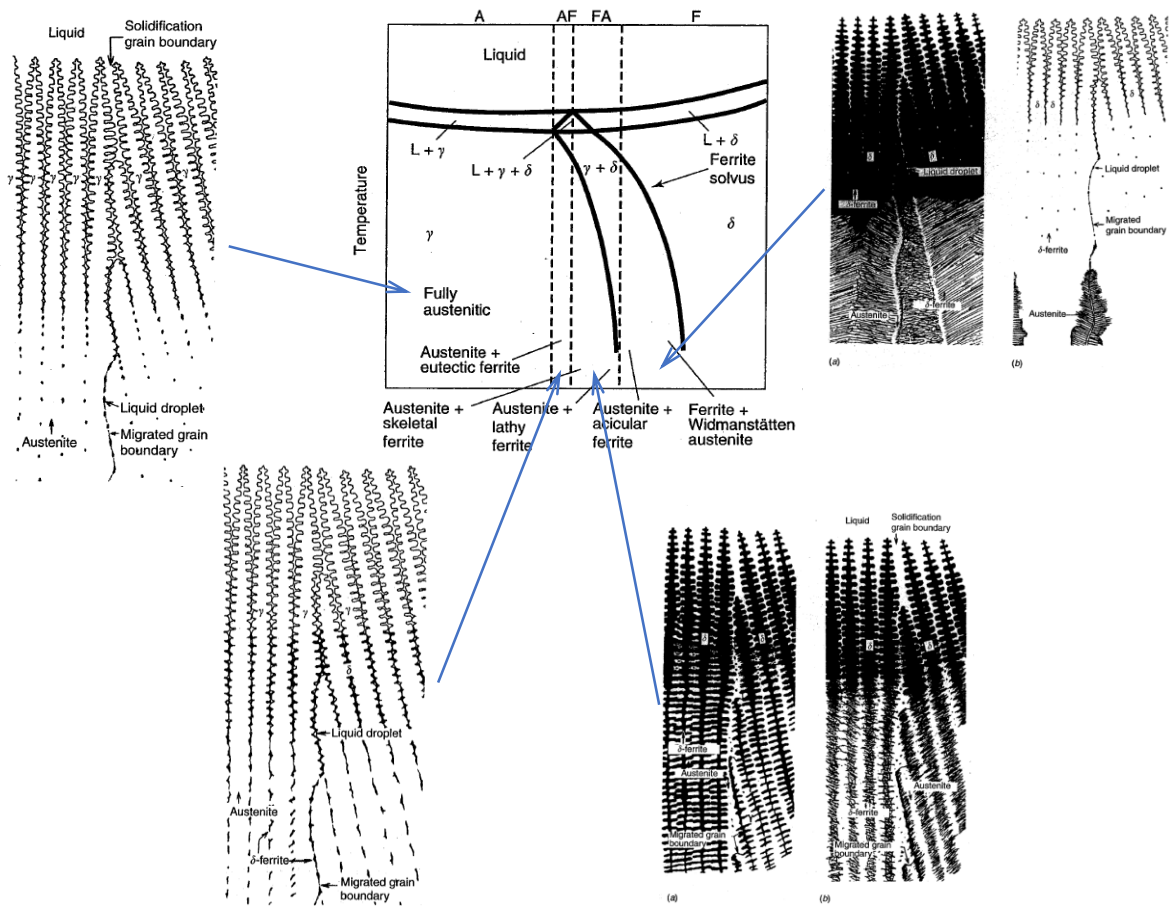


Figure 3.4: solidification modes found in austenitic SS welds [adapted from 29]

The different solidification options highlighted in figure 3.2 result in distinct solidification microstructures and solid-state transformation sequences for austenitic SS welds, according to the schematic representation supplied in figure 3.4.

- A: solidification as primary austenite; segregation of Cr and Mo at GBs is not significant to nucleate new phases, a fully austenitic structure results,
- AF: ferrite forms at end of solidification process (eutectic reaction) due to partition of Cr and Mo to the subgrain boundaries,
- FA: solidification as primary ferrite with subsequent austenite formed at end of solidification via peritectic-eutectic reaction or during solid state cooling (ferrite results with skeletal or lathy shape),
- F (very unusual in austenitic SS): fully ferritic solidification followed by partial solid-state transformation into austenite (the degree of transformation depends on Cr_{eq}/Ni_{eq} and on cooling rate) resulting in acicular ferrite or ferrite + Widmanstätten austenite).

Additional effects brought by welding are expected in the HAZ such as grain coarsening (usually not dramatic) due to thermal cycles, further δ -ferrite precipitation that was prevented by prior fast cooling, precipitation of secondary phases especially carbides and nitrides, grain boundary liquation (cracking) promoted by segregation of impurities that reduce the melting temperature.

Finally, it must be considered that most of the transformations above described occur at very high temperatures, where pre-heat and interpass temperature control have little effects. Contrarily, post-weld treatments are sometimes used in thick parts to relieve residual stresses. Annealing is performed in the range 550-650°C where precipitation of carbides is rather slow. Precipitation of sigma phase is of concern only in SS containing significant amounts of ferrite. Keeping the amount of ferrite to a limited extent (FN in the range 3-8) is usually enough to avoid embrittlement.

Weldability of austenitic SS is generally considered as good. However, some concerns about weld metal solidification cracking and liquation cracking may arise when the impurity level

(especially S and P) is significantly high. Cracking susceptibility is strongly enhanced by type A solidification mode, whereas type FA tends to be very resistant to cracking [29,30].

It is demonstrated that the weld cracking susceptibility depends primarily on Cr_{eq}/Ni_{eq} and on the impurity level, according to the Suutala diagram, as depicted in figures 3.5 and 3.6.

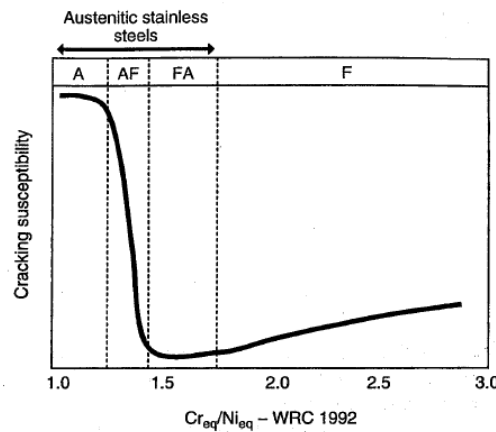


Figure 3.5: weld metal solidification cracking susceptibility as a function of steel composition [29]

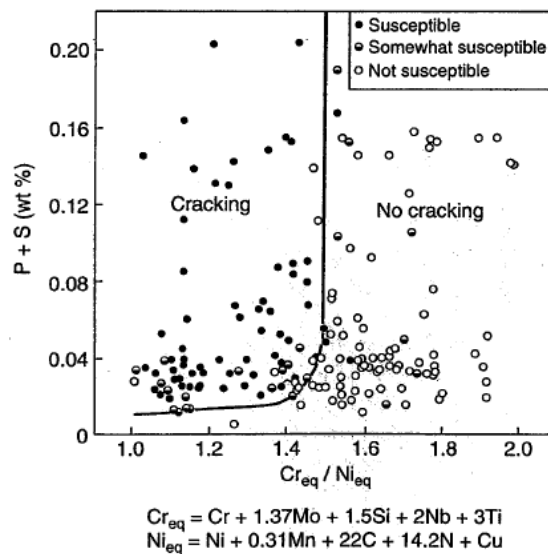


Figure 3.6: Suutala diagram for predicting the solidification cracking from weld metal composition [30]

The beneficial effect of a fair content of residual ferrite at room temperature deriving from the FA-type solidification mode can be summarized according to the following aspects:

- δ -ferrite has a higher solubility for impurities (S + P) which restricts segregation,
- wetting by liquid melt is lower at F-F and F-A interfaces than for A-A boundaries,
- The mixed A+F structure promotes tortuous boundaries that hinder crack growth,

- δ -ferrite has improved high-temperature ductility and lower CTE than γ -austenite.

As a result, a ferrite content (FN) in the range 3-8 is considered as optimal for austenitic SS welds.

3.2 Literature survey on LBW of austenitic stainless steels

Effect of rapid cooling on solidification conditions

Further consideration has to be given to the effect of rapid solidification conditions, as induced by LBW when compared to more traditional welding processes, such as several arc welding methods on which the previous introductory overview was based.

Already in 1994 Lippold [30] understood that rapid solidification conditions such as those met in LBW promote a shift in the boundaries of the solidification modes. The published results showed that under rapid solidification, dendrite tip undercooling increased the stability of austenite relative to ferrite, leading to a shift in the critical value of the Cr_{eq}/Ni_{eq} required to promote primary ferrite solidification, as depicted in figure 3.7.

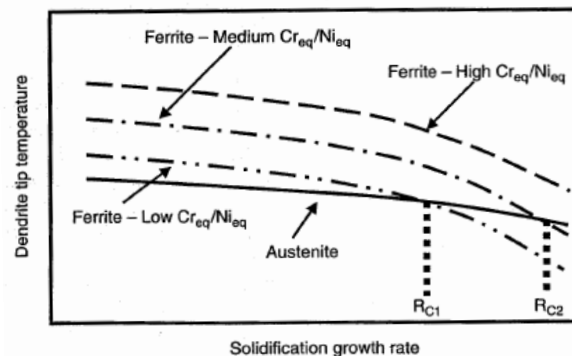


Figure 3.7: effect of rapid solidification on dendrite tip undercooling [29]

As a result, alloys that are crack resistant under normal welding conditions may become crack sensitive in LBW due to this shift in solidification mode (see figure 3.8). An updated map of the solidification mode was therefore proposed to account for the different solidification rates encountered in distinct welding processes, as shown in figure 3.9 [30].

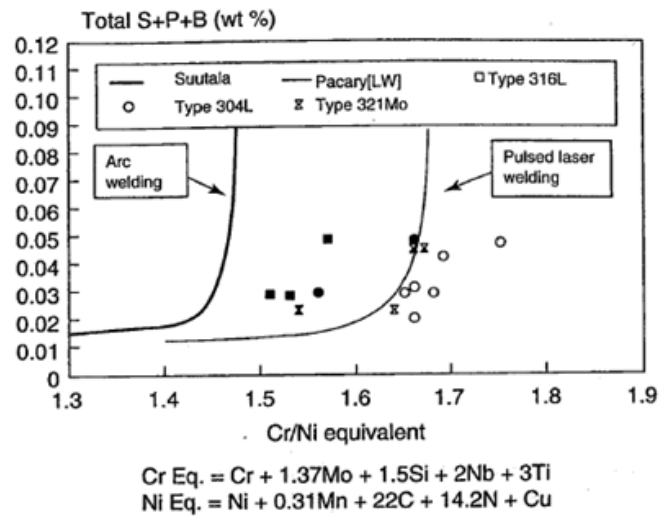


Figure 3.8: shift of solidification mode boundaries for pulsed laser welding processes [30]

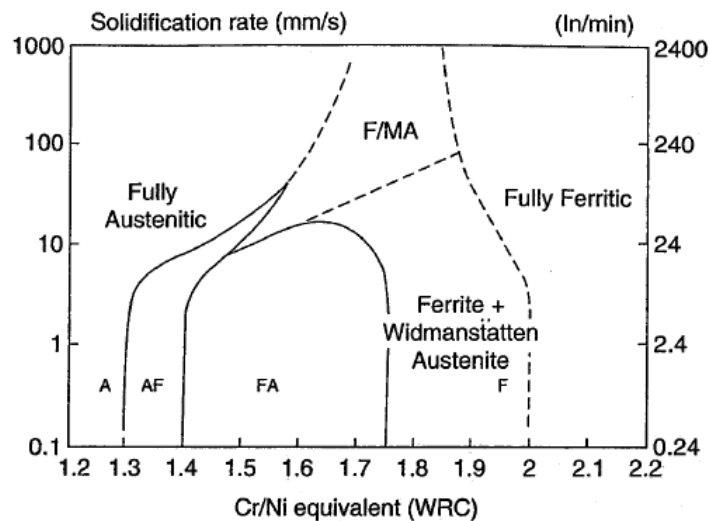


Figure 3.9: microstructural map of weld metal constituents as a function of solidification rate and composition [30]

Numerical analyses about LBW processing

Numerical models have been presented in literature to compute thermal profiles and resulting shape of the melt pool during welding of fairly thin steel sheets. In [31] a 3D finite element method (FEM) model was developed using the ANSYS code to predict butt-joint laser welding of 2,5 mm thick AISI 304 sheets, while in [32] similar models based both on finite difference model (FDM) and FEM are introduced to simulate a pulsed laser source producing seam welding on 1 mm thick sheets of low-C steel.

There is general evidence that temperature-dependent material thermo-physical properties should be correctly considered in models. The effects of latent heat and of convective and radiative conditions also need to be correctly evaluated and modelled [31]. Both models supplied maps and profiles of temperature as well as information on weld pool shape and size as a function of LBW parameters. Evaluation of HAZ is also possible.

Experimental investigations on LBW processing and weld cracking

In reference [33] bead-on-plate welds were produced on AISI 304 SS under different conditions to investigate the effects of process parameters. Table 3.2 summarizes the ranges of parameter investigated, whereas in figure 3.10 a collection of images of the weld cross-sections is given as a function of the adopted processing conditions.

Table 3.2: laser welding parameters adopted [31]

Laser welding conditions	Values
Laser power	3~6 kW
Weld speed	1~8 m/ min
Focus Position	±20m m
Gas	Ar, Ar+N ₂ , N ₂
Gas flow rate	30~50 L/min

Welding at defocus positions produced different shapes of molten pools, ranging between wide & shallow welds (conduction mode) and narrow & deep welds (keyhole mode). Neither laser power nor welding speed have noticeable effects on the microstructure of the weld zone. The higher the welding speed, the finer the dendrite structure due to the increasing in cooling rate. The shielding gas could decrease the ferrite number from 4.25 in 100% Ar to 3.13 in 100% N₂.

Further observation of weld bead surfaces allowed to define that at high welding speed (10 m/min) the weld beads were unstable with spatters in all the laser power range due to the shorter molten pool and instability of the keyhole. At low speed (6 m/min) full penetration welds and stable beads were obtained.

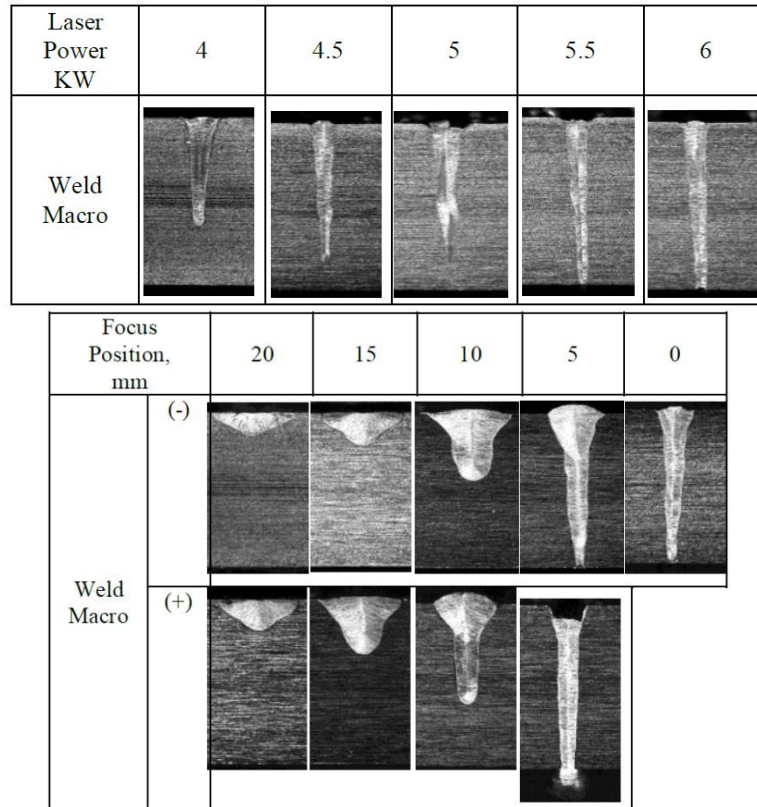


Figure 3.10: cross sections of weld beads produced by various laser parameters [33]

Specific conditions leading to weld cracking are presented in [34,35] for the production of 304 and 304L SS joints. The research carried out at Los Alamos National Laboratories concerns annular welds made between coaxial tubes of 304 and 304L SS by Nd:YAG pulsed LBW or gas tungsten arc welding (GTAW). The chemical compositions of the steels investigated is reported in table 3.3.

Table 3.3: chemical compositions of the steels investigated in [34]

	Outer Tube (304L)	Inner Tube (304)
Cr	18.5	19.9
Ni	11.6	10.0
Mn	1.6	1.8
Si	0.36	0.46
Co	0.025	N/A
Mo	0.044	N/A
C	0.027	0.051
S	0.002	0.016
P	0.010	0.020
N	0.037	N/A
Hammar and Svensson Cr _{eq} /Ni _{eq}	1.44	1.72
S+P	0.012	0.036

As depicted in figure 3.11, conditions were met, especially at higher heat input, that generated extensive cracking in the weld zone. Changes in local solidification mode were observed based on microstructure of cross sectioned joints (figure 3.11b). Cracks were more frequent in LBW but critical conditions were found also in GTAW. This suggests that cooling rate plays a role on solidification mode. It was estimated that LBW gives cooling rates in the range of 10^5 - 10^6 K/s while GTAW is in the range 10^3 - 10^4 K/s.

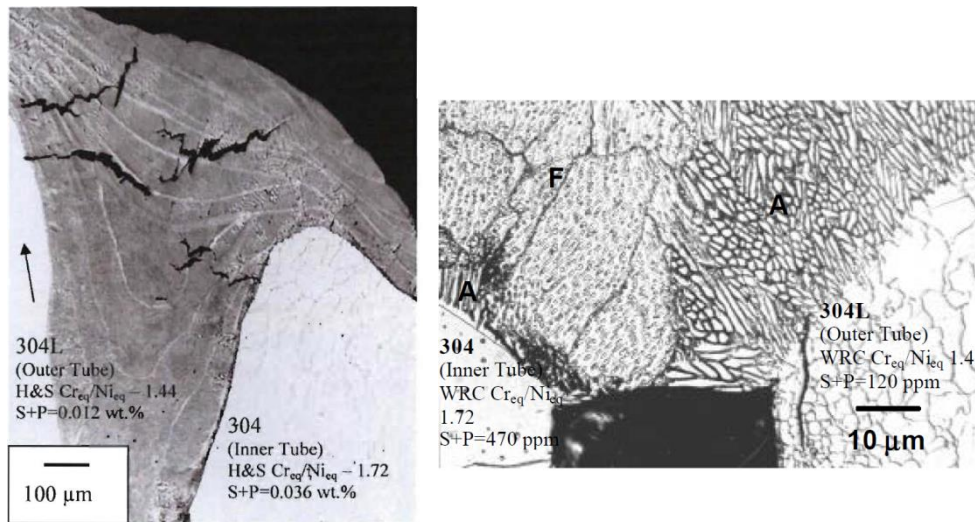
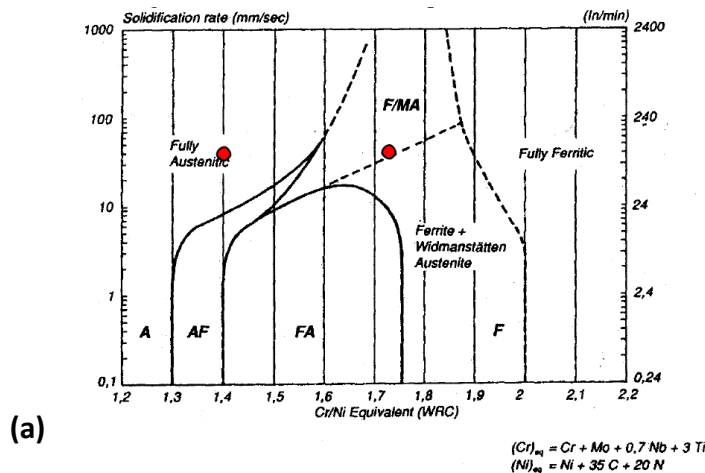


Figure 3.11: solidification cracking in LBW of 304/304L SS; (a) general view of weld bead, (b) detail about evidence of variation in solidification mode at the root of the weld [34]

It was speculated that the different solidification modes could be justified based on prediction maps, already presented in [30], as shown in figure 3.12.



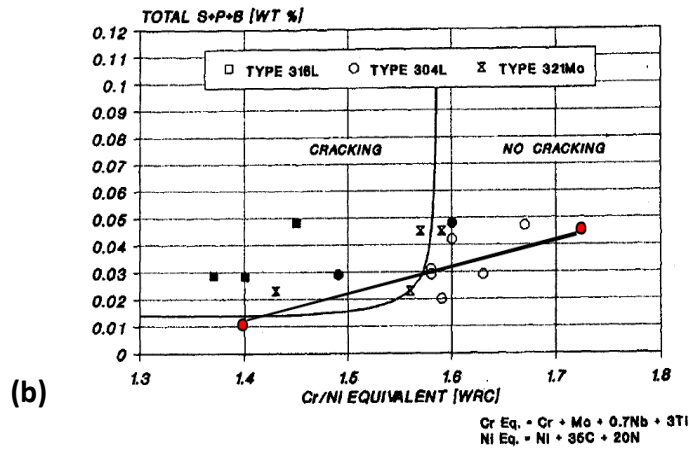


Figure 3.12: solidification map showing (a) the expected fields for the two steels investigated and (b) the tie line the two compositions that can cross the cracking zone for specific mixtures of the two alloys [34]

The study presented by Kumar and co-authors in [36] proposes a comparison of pulsed Nd:YAG laser welds of type 304 and 316 SS. Butt welded joints were produced by a 600 W laser on 1,5 mm thick sheets. Based on the different chemistry ranges of the two grades, the following solidification modes are expected:

- 316 SS: $1,25 < Cr_{eq}/Ni_{eq} < 1,48$, AF solidification mode: $L \rightarrow L+\gamma \rightarrow L+\gamma+\delta \rightarrow \gamma+\delta \rightarrow \gamma$
- 304 SS: $1,48 < Cr_{eq}/Ni_{eq} < 1,95$, FA solidification mode: $L \rightarrow L+\delta \rightarrow L+\delta+\gamma \rightarrow \delta+\gamma \rightarrow \gamma$

A wide set of welding parameters were investigated. Significant differences in net energy inputs led to variations in cooling rates (see figure 3.13), grain structure in the fusion zone and related modifications of hardness and tensile strength (see figure 3.14).

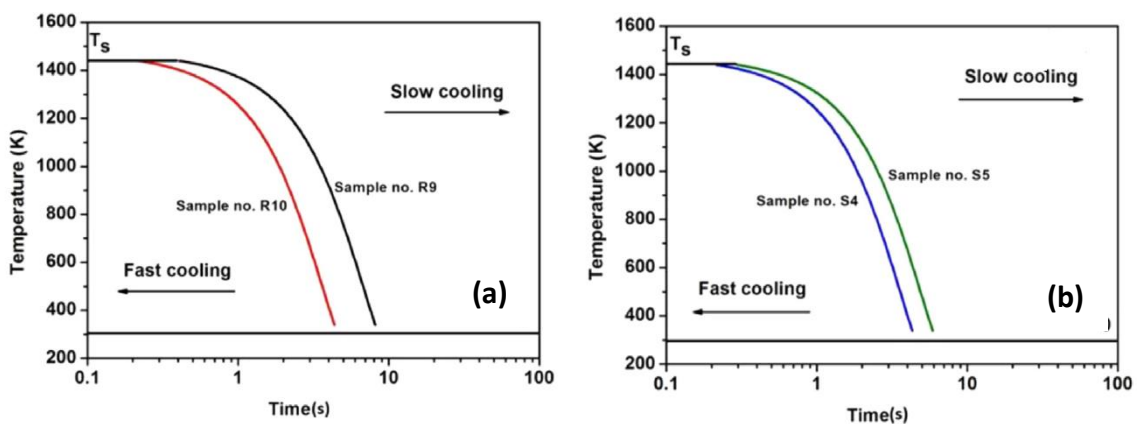


Figure 3.13: calculated cooling curve ranges for the 304 (a) and 316 (b) SS weld samples according to the investigated laser weld parameters [36]



Sample Specification	σ_{YS} (MPa)	σ_{UTS} (MPa)	e_u (%)	Location of fracture
BM 304SS	302.06	632.67	49.77	BM
R9	270.87	388.15	5.045	WM
R10	284.41	681.5	44.83	HAZ/BM
BM 316SS	235.56	617.05	31.81	BM
S4	324.51	600.21	34.27	HAZ/BM
S5	274.35	361.43	2.61	WM

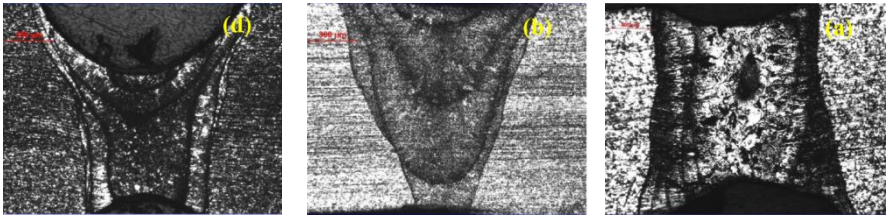


Figure 3.14: tensile properties of parent and welded joints produced according to different parameters [adapted from 36]



4 CONCLUSIONS

In the present handbook information are collected on the features and mechanisms of generation of metallurgical defects found in laser powder bed fusion (LPBF) and laser beam welding (LBW). Focus is mainly given on the reference materials selected for the CUSTODIAN project activities, namely the CM247LC and IN713LC alloys for LPBF and the AISI 304L austenitic stainless steel for LBW. Data are obtained from a literature survey on available open publications.

The selection of discussed papers was carried out considering the need to acquire fundamental knowledge on metallurgical principles governing the processes and the defect generation in LPBF and LBW. General data about the reference materials were also summarized and discussed to make them available for future model development and to support analyses of experimental results planned in the frame of the project.

5 REFERENCES

- [1] R.C. Reed, C.M.F. Rae. Physical metallurgy of the Nickel-based superalloys. Physical Metallurgy (fifth edition), Ed. D.E. Laughlin and K. Hono, Elsevier Publ. (2015) 2215-2290
- [2] T. DebRoy, H.L. Wei, J.S. Zuback, T. Mukherjee, J.W. Elmer, J.O. Milewski, A.M. Beese, A. Wilson-Heid, A. De, W. Zhang. Additive manufacturing of metallic components – Process, structure and properties. Progress in Materials Science 92 (2018) 112–224
- [3] S. Kou. Welding Metallurgy, John Wiley & Sons Publ. (2002)
- [4] ASM Handbook. Vol. 1, Properties and Selection: Irons, steels and high-performance alloys. ASM International Publ. (2005) online ed.
- [5] H.-E. Huang, C.-H. Koo. Characteristics and Mechanical Properties of Polycrystalline CM247LC Superalloy Casting. Materials Transactions, Vol. 45, No. 2 (2004) 562-568
- [6] M. B. Henderson, D. Arrell, R. Larsson, M. Heobel & G. Marchant. Nickel based superalloy welding practices for industrial gas turbine applications. Science and Technology of Welding and Joining, 9 (2004) 13-21
- [7] G. Çam & M. Koçak. Progress in joining of advanced materials. International Materials Reviews, 43 (1998) 1-44
- [8] L.N. Carter, M.M. Attallah, R.C. Reed. Laser Powder Bed Fabrication of Nickel-Base Superalloys: Influence of Parameters; Characterisation, Quantification and Mitigation of Cracking. 12th International Symposium on Superalloys. Ed. E.S. Huron, R.C. Reed, M.C. Hardy, M.J. Mills, R.E. Montero, P.D. Portella, J. Telesman. TMS Publ. (2012) 577-586
- [9] P. Jonšta, Z. Jonšta, J. Sojka, L. Čížek, A. Hernas. Nickel super alloy IN713LC – structural characteristics after heat treatment. Journal of Achievements in Materials and Manufacturing Engineering. 22 (2007) 7-14
- [10] P. Jonšta, Z. Jonšta, J. Sojka, L. Čížek, A. Hernas. Structural characteristics of nickel super alloy IN713LC after heat treatment. Journal of Achievements in Materials and Manufacturing Engineering. 21 (2007) 29-32
- [11] A.Chamanfar, M.Jahazi, A.Bonakdar, E.Morin, A.Firoozrai. Cracking in fusion zone and heat affected zone of electron beam welded Inconel-713LC gas turbine blades. Materials Science & Engineering, A642 (2015) 230–240

- [12] M.K. Keshavarz, S. Turenne, A. Bonakdar. Solidification behavior of inconel 713LC gas turbine blades during electron beam welding. *Journal of Manufacturing Processes*, 31 (2018) 232–239
- [13] S. Zla, B. Smetana, M. Zaludova, J. Dobrovska, V. Vodarek, K. Konecna, V. Matejka, H. Francova. Determination of thermophysical properties of high temperature alloy IN713LC by thermal analysis. *Journal of Thermal Analysis and Calorimetry*, 110 (2012):211–219
- [14] L.N. Carter, C.Martin, P.J. Withers, M.M. Attallah. The influence of the laser scan strategy on grain structure and cracking behaviour in SLM powder-bed fabricated nickel superalloy. *Journal of Alloys and Compounds* 615 (2014) 338–347
- [15] V.D. Divya, R. Muñoz-Moreno, O.M.D.M. Messé J.S. Barnard, S. Baker, T. Illston, H.J. Stone. Microstructure of selective laser melted CM247LC nickel-based superalloy and its evolution through heat treatment. *Materials Characterization* 114 (2016) 62–74
- [16] H. Peng, Y. Shi, S. Gong, H. Guo, B. Chen. Microstructure, mechanical properties and cracking behaviour in a γ' -precipitation strengthened nickel-base superalloy fabricated by electron beam melting. *Materials and Design* 159 (2018) 155–169
- [17] E. Chauvet, C. Tassin, J.-J. Blandin, R. Dendievel, G. Martin. Producing Ni-base superalloys single crystal by selective electron beam melting. *Scripta Materialia* 152 (2018) 15–19
- [18] E. Chauvet, P. Kontis, E.A. Jågle, B. Gault, D. Raabe, C. Tassin, J.-J. Blandin, R. Dendievel, B. Vayre, S. Abed, G. Martin. Hot cracking mechanism affecting a non-weldable Ni-based superalloy produced by selective electron Beam Melting. *Acta Materialia* 142 (2018) 82-94.
- [19] W.J. Sames, K.A. Unocic, G.W. Helmreich, M.M. Kirka, F. Medina, R.R. Dehoff, S.S. Babu. Feasibility of in situ controlled heat treatment (ISHT) of Inconel 718 during electron beam melting additive manufacturing. *Additive Manufacturing* 13 (2017) 156–165
- [20] V. Manvatkar, A. De, and T. DebRoy. Heat transfer and material flow during laser assisted multi-layer additive Manufacturing. *Journal of Applied Physics*, 116 (2014) 124905
- [21] H.L. Wei, G.L. Knapp, T. Mukherjee, T. DebRoy. Three-dimensional grain growth during multi-layer printing of a nickel based alloy Inconel 718. *Additive Manufacturing* 25 (2019) 448–459

- [22] Y. Yang, F. Van Keulen, C. Ayas. A computationally efficient thermal model for selective laser melting. Additive Manufacturing (2019) preprint, doi: 10.1016/j.addma.2019.100955
- [23] Y. Du, X. You, F. Qiao, L. Guo, Z. Liu. A model for predicting the temperature field during selective laser melting. Results in Physics 12 (2019) 52–60
- [24] Y. Li, D. Gu. Thermal behavior during selective laser melting of commercially pure titanium powder: Numerical simulation and experimental study. Additive Manufacturing 1–4 (2014) 99–109
- [25] Y. Li, K. Zhou, P. Tan, S.B. Tor, C.K. Chua, K.F. Leong. Modeling temperature and residual stress fields in selective laser melting. International Journal of Mechanical Sciences 136 (2018) 24–35
- [26] G.L. Knapp, N. Raghavan, A. Plotkowski, T. DebRoy. Experiments and simulations on solidification microstructure for Inconel 718 in powder bed fusion electron beam additive manufacturing. Additive Manufacturing 25 (2019) 511–521
- [27] H. Peng, M. Ghasri-Khouzan, S. Gong, R. Attardo, P. Ostiguy, B. Aboud Gatrell, J. Budzinski, C. Tomonto, J. Neidig, M. Ravi Shankar, R. Billo, D.B. Go, D. Hoelzle. Fast prediction of thermal distortion in metal powder bed fusion additive manufacturing: Part 1, a thermal circuit network model. Additive Manufacturing 22 (2018) 852–868
- [28] H. Peng, Morteza Ghasri-Khouzani, S. Gong, R. Attardo, P. Ostiguy, R.B. Rogge, B.A. Gatrell, J. Budzinski, C. Tomonto, J. Neidig, M. Ravi Shankar, R. Billo, D.B. Go, D. Hoelzle. Fast prediction of thermal distortion in metal powder bed fusion additive manufacturing: Part 2, a quasi-static thermo-mechanical model. Additive Manufacturing 22 (2018) 869–882
- [29] J. Lippold, D.J. Kotecki. Welding Metallurgy and Weldability of Stainless Steels. J. Wiley Publisher (2005) 141–229
- [30] J.C. Lippold. Solidification Behavior and Cracking Susceptibility of Pulsed-Laser Welds in Austenitic Stainless Steels. Welding Research Supplement of Welding Journal, 6 (1994) 129s – 139s
- [31] N. Siva Shanmugam, G. Buvanashakaran, K. Sankaranarayanan, K. Manonmani. Some studies on temperature profiles in AISI 304 stainless steel sheet during laser beam

welding using FE simulation. *International Journal of Advanced Manufacturing Technologies*, 43 (2009) 78–94

[32] J. Sabbaghzadeh, M. Azizi, M.J. Torkamany. Numerical and experimental investigation of seam welding with a pulsed laser. *Optics & Laser Technology* 40 (2008) 289–296

[33] K.M. Hafez, S. Katayama. Fiber laser welding of AISI 304 stainless steel plates. *Quarterly Journal of the Japan Welding Society*, 1 (2009) 1-5

[34] P.W. Hochanadel, M.J. Cola, A.M. Kelly, P.A. Papin. Pulsed Laser Beam Welding of 304 to 304L Stainless Steel: Effects of Welding Parameters on Cracking and Phase Transformations. Los Alamos National Laboratory Public report LA-UR-01-6144, Proceedings of Joining of Advanced and Specialty Materials IV, Indianapolis, Indiana, ASM International Publisher (2001) pp. 16–21

[35] P. Hochanadel, T. Lienert, R. Martinez, J. Martinez, M. Johnson. Weld Solidification Cracking in 304 to 304L Stainless Steel. Los Alamos National Laboratory Public report LA-UR-10-04375. In: *Hot Cracking Phenomena in Welds III*. T. Böllinghaus, J. Lippold, C. Cross. Editors, Springer Publisher (2011) 145-160

[36] Comparative study of pulsed Nd:YAG laser welding of AISI 304 and AISI 316 stainless steels. N. Kumar, M. Mukherje, A. Bandyopadhyay. *Optics & LaserTechnology*, 88 (2017) 24–39